Effect of saturation temperature on the condensation of R134a inside an inclined smooth tube

S. M. A. Noori Rahim Abadi*, M. Mehrabi, Josua P. Meyer, J. Dirker

Department of Mechanical and Aeronautical Engineering, University of Pretoria, Pretoria, South Africa

*Corresponding author. Tel.: +27 12 420 3104

E-mail address: ali.abadi@up.ac.za

Highlights

- Effect of the inclination angle on the heat transfer coefficient and pressure drop.
- Condensation heat transfer coefficient increased with increasing mass flux and vapour quality.
- Condensation heat transfer coefficient increased with the decrease in saturation temperature.
- Pressure drop along the tube increased with the decrease in saturation temperature.
- An optimum inclination-angle-region of $-30\ ° < \beta < -15°$ was observed in the simulation.

Abstract

In this study, numerical simulations of the condensation of R134a inside an inclined smooth tube are conducted. The effects of different parameters such as saturation temperature, tube inclination angle, vapour quality, and mass flux, on variations of the condensation heat transfer coefficient and pressure drop along the tube were investigated. The simulations were performed at a uniform heat flux of 5050 W/m^2, mass fluxes of 100 – 400 kg/m^{2}s, saturation temperatures of 30 – 50 °C, vapour qualities of 0.1 – 0.9, and inclination angles of -90 – +90°. It was assumed that the flow field was three-dimensional, transient, and turbulent. The volume of fluid model was used to solve the governing equations. The simulated results for the condensation heat transfer coefficient and pressure drop showed good correlation with the available experimental data. The results also demonstrated that the condensation heat transfer coefficient and pressure drop along the tube increased with decreasing saturation temperature, and increasing mass flux and vapour qualities. It was also determined that there was an optimum inclination-angle-range, -30 – -15°, in which the condensation heat transfer coefficient attained a maximum value.

Keywords: Condensation, Inclination angle, VOF, Pressure drop, Saturation temperature.

1. Introduction

Condensation inside tubes can be observed in numerous industries and applications such as power plants, desalination, refrigeration, and heat exchangers. Accurately understanding the condensation phenomenon, and the primary effective parameters in these applications, will result in enhanced efficiency and performance of systems.

In numerous applications, the tubes are positioned horizontally or vertically; however, there are specific cases where the tubes are placed in an inclined position. Previous studies

demonstrated that the imposed inclination angle would result in significant changes in the heat transfer rate, pressure drop, and flow regime inside the tube (Adelaja *et al.*, 2016).

During the last few years, Meyer and his co-workers (Adelaja *et al.*, 2017; Lips and Meyer, 2012a, b, c; Lips and Meyer, 2012d; Meyer *et al.*, 2014) conducted extensive experimental studies on the condensation of R134a inside an inclined smooth tube. They considered the effect of numerous critical parameters such as refrigerant mass flux, vapour quality, saturation temperature, and tube orientation, on the condensation heat transfer coefficient, pressure drop, and flow regime inside the tube. They determined that the effect of the inclination angle on the heat transfer coefficient and pressure drop is considerable at low mass fluxes and vapour qualities. One of their most critical observations, was that of an optimum inclination angle region, from -30 – -15°, in which the heat transfer coefficient is maximum. The exact position of the optimum point was dependent on the mass flux and vapour quality.

Kang *et al.* (2017) performed an experimental investigation to study the effect of tube orientation on the pressure drop and flow regime during the condensation of steam inside an inclined channel, and reported that their results differed significantly from the available experimental correlations.

One of the most referred-to studies on condensation inside tubes and channels was conducted by Shah (1987). He proposed and developed straightforward and accurate correlations for the prediction of condensation heat transfer coefficients inside tubes and channels. His correlations were primarily based on the flow regimes inside the tubes, and recently, he updated his proposed correlations to consider the effect of tube inclination angles (Shah, 2016a; Shah, 2016b, c).

Park *et al.* (2017) and O'Neill *et al.* (2017) studied the condensation of FC-72 inside an inclined smooth tube, and published their works in a two-part article. They determined that inclining the tube at low mass fluxes resulted in an increased condensation heat transfer coefficient, whereas, at higher mass fluxes, it did not have a considerable influence. They also proposed a mathematical expression for predicting the condensation heat transfer coefficient in stratified flow regimes (O'Neill *et al.*, 2017). They validated the proposed model with their experimental data. Based on the results of the proposed model and experiments, they determined that at low mass velocities, the gravitational force plays a dominant role in the condensation phenomenon compared to the wall and interfacial shear forces.

Col *et al.* (2014) investigated the effect of inclination angle on the condensation of R134a inside a square cross-section mini-channel at a saturation temperature of 40 °C. By using the Buckingham theorem, they introduced a criterion to predict the mass flux at which the inclination angle will begin to affect the condensation heat transfer coefficient.

Because of the diverse applications in the refrigeration and air conditioning industries, the effects of tube geometry and orientation on the condensation heat transfer coefficient, and pressure drop, have received considerable attention over the past few years (Darzi *et al.*, 2015; Kaew-On *et al.*, 2016; Nebuloni and Thome, 2013; Wen *et al.*, 2018; Yildiz *et al.*, 2017). Wen *et al.* (2018) studied the condensation of R134a inside flattened tubes numerically. The results showed that the condensation heat transfer coefficient increased with increasing vapour quality and tube aspect ratio. They also proposed a correlation for predicting the condensation heat transfer coefficient inside flattened tubes. They reported that the differences between the predicted results and experimental data were less than 15%.

One of the most important issues regarding condensation inside tubes, is to comprehensively understand the flow patterns under different operating conditions, as it is an effective parameter in determining the condensation heat transfer coefficient and pressure drop. Numerous researchers have conducted experiments to determine the flow regimes based on the refrigerant mass flow rates, saturation temperatures, and vapour qualities (Tao *et al.*, 2018; Vanderputten *et al.*, 2017; Zhuang *et al.*, 2017).

Studies regarding the inclination effect on the condensation heat transfer coefficient have been conducted, primarily involving experimentation (Beggs and Brill, 1973; Caruso *et al.*, 2012; Caruso *et al.*, 2013; Chato, 1962; Diani *et al.*, 2017; Jr. *et al.*, 2015). Although there have been studies conducted on the numerical simulation of condensation inside tubes (Behafarid *et al.*, 2015; Bortolin *et al.*, 2014; Höhne *et al.*, 2011; Kouhikamali, 2010; Lin *et al.*, 2013; Nebuloni and Thome, 2010, 2012; Riva and Col, 2009), they were limited to vertical or horizontal tubes. Nebuloni and Thome (2010) proposed a numerical model, based on the finite volume method, to predict the film condensation heat transfer in mini- and micro-channels with different internal shapes. Their method was limited to the laminar annular flow regime in horizontal and vertical channels. They reported that the geometrical shape, in conjunction with the capillary forces, could significantly enhance the overall thermal performance. Kouhikamali (2010) used the volume of fluid (VOF) method to simulate the condensation of steam inside a horizontal tube. His results showed that the condensation heat transfer coefficient and condensation length increased with increasing inlet steam Reynolds number, and a decreasing temperature difference between the wall and saturated steam. Bortolin *et al.* (2014) studied the condensation of R134a inside a rectangular cross-sectioned mini-channel channel numerically. They found that the effect of surface tension on the shape of the liquid-vapour interface could result in an increase in the condensation heat transfer enhancement, particularly at low mass fluxes.

The literature review revealed that there are no published numerical studies where the effect of tube orientation on the condensation phenomenon have been investigated. However, as discussed above, this effect can result in a considerable increase in the condensation heat transfer coefficients and could be of significant interest in the context of heat exchanger design, as the increase can be achieved without additional cost. Therefore, the objective of this study is to study the effect of inclination angle on the condensation heat transfer coefficient, pressure drop, and flow regime inside an inclined smooth tube. In this study, the effects of various parameters such as saturation temperature, vapour quality, and mass flux, are taken into account. Furthermore, the effect of these parameters on the liquid film thickness, and inter-phase forces are also studied.

2. Mathematical Formulations

In this study, the VOF multiphase flow model that has been proven by numerous researchers to accurately capture the liquid-vapour interface, particularly in separated flow patterns (Bortolin *et al.*, 2014; Lee, 1980; Liu *et al.*, 2012; Taha and Cui, 2006), is used for the simulation of the condensation of R134a inside an inclined tube. In this model, the governing equations, i.e. continuity, momentum, and energy equations, are defined as follows (Hirt and Nichols, 1981):

$$\frac{\partial \alpha_v}{\partial t} + \nabla.(\vec{u}\alpha_v) = \frac{S_v}{\rho_v} \tag{1}$$

$$\frac{\partial \alpha_l}{\partial t} + \nabla.(\vec{u}\alpha_l) = \frac{S_l}{\rho_l} \tag{2}$$

$$\frac{\partial(\rho_m \vec{u})}{\partial t} + \nabla.(\rho_m \vec{u}\vec{u}) = -\nabla p + \nabla.[\mu_{m,eff}(\nabla\vec{u} + (\nabla\vec{u})^T)] + \rho_m \vec{g} + \vec{F}_\sigma \tag{3}$$

$$\frac{\partial(\rho_m E)}{\partial t} + \nabla.[\vec{u}(\rho_m E + p)] = \nabla.(k_{m,eff}\nabla T) + S_E \tag{4}$$

where α is the volume fraction; $\vec{u}$ is the velocity; t is time; parameter S is the source term from a phase change; indices l, v, and, m are the liquid, vapour, and mixture phases, respectively; and μ_{eff}, k_{eff}, g, p, ρ, E, and F_σ are the effective viscosity, effective thermal conductivity, gravitational acceleration, pressure, density, internal energy, and surface tension force, respectively.

The average phase properties of the mixture are defined as follows:

$$\begin{aligned} k_m &= \alpha_l k_l + \alpha_v k_v \\ \rho_m &= \alpha_l \rho_l + \alpha_v \rho_v \\ \mu_m &= \alpha_l \mu_l + \alpha_v \mu_v \end{aligned} \tag{5}$$

The effective parameters, μ_{eff} and k_{eff}, are the summation of the laminar and turbulent properties and can be defined as follows:

$$\begin{aligned} \mu_{eff} &= \mu_L + \mu_t \\ k_{eff} &= k_L + k_t \end{aligned} \tag{6}$$

Where μ_L and μ_t, and k_L and k_t are the laminar and turbulent dynamic viscosity and thermal conductivity, respectively.

In the present study, the surface tension force, F_σ, which acts in the tangential direction at the interface is calculated based on the continuum surface force (CSF) model proposed by Brackbill *et al.* (1992) as:

$$\vec{F}_{\sigma} = \sigma \frac{\alpha_l \rho_l k_v \nabla \alpha_v + \alpha_v \rho_v k_l \nabla \alpha_l}{\frac{1}{2}(\rho_v + \rho_l)} \tag{7}$$

where σ is the surface tension. The curvatures of the liquid and vapour phases, k_l and k_v, are calculated as follows:

$$k_l = \nabla . \frac{\nabla \alpha_l}{|\nabla \alpha_l|}, \quad k_v = \nabla . \frac{\nabla \alpha_v}{|\nabla \alpha_v|} \tag{8}$$

In this work, a two-equation standard k-ε turbulence model, is used for modelling the turbulence. The governing equations in this model are presented as (Yang and Shih, 1993):

$$\frac{\partial(\rho_m k)}{\partial t} + \nabla.(\rho_m \vec{u} k) = \nabla.[(\mu_{L,m} + \frac{\mu_{t,m}}{\sigma_k})\nabla k] + [\mu_{t,m}(\nabla \vec{u} + (\nabla \vec{u})^T) : \nabla . \vec{u}] - \rho_m \varepsilon + G_b \tag{9}$$

$$\begin{aligned} \frac{\partial(\rho_m \varepsilon)}{\partial t} + \nabla.(\rho_m \vec{u} \varepsilon) = \nabla.[(\mu_{L,m} + \frac{\mu_{t,m}}{\sigma_\varepsilon})\nabla \varepsilon] \\ + \frac{\varepsilon}{k}(C_{1\varepsilon}[\mu_{t,m}(\nabla \vec{u} + (\nabla \vec{u})^T) : \nabla . \vec{u}] - C_{2\varepsilon} \rho_m \varepsilon) + C_{1\varepsilon} C_{3\varepsilon} \frac{\varepsilon}{k} G_b \end{aligned} \tag{10}$$

where k and ε, and G_b are respectively the turbulent kinetic energy, turbulent energy dissipation rate, and generation of turbulence kinetic energy due to buoyancy. Furthermore, the turbulent viscosity, $\mu_{t,m}$, is defined as follows (Yang and Shih, 1993):

$$\mu_{t,m} = C_\mu \frac{\rho_m k^2}{\varepsilon} \tag{11}$$

The constants in the standard k-ε model are defined as (Yang and Shih, 1993):

$$C_{\mu}=0.09, C_{1\varepsilon}=1.44, C_{2\varepsilon}=1.92, C_{3\varepsilon}=tanh\left|\frac{v}{u}\right|, \sigma_{k}=1.0, \sigma_{\varepsilon}=1.3 \tag{12}$$

Further details of the parameters used in the turbulence model are available in (Yang and Shih, 1993).

In this study, the mass transfer rate due to the condensation phenomenon is calculated as (Liu *et al.*, 2012):

$$S_{l}=r_{l}\alpha_{l}\rho_{l}\frac{T-T_{sat}}{T_{sat}} \quad if \quad T\geq T_{sat} \tag{13}$$

$$S_{v}=r_{v}\alpha_{v}\rho_{v}\frac{T_{sat}-T}{T_{sat}} \quad if \quad T<T_{sat} \tag{14}$$

where T and T_{sat} are the fluid temperature and saturation temperature, respectively. The parameters, r_l and r_v, should be tuned in a way that two goals are obtained. The first one is to attain the interface temperature as much as possible close to the saturation temperature. The second goal is to achieve the correct value of the condensation heat transfer coefficient compared to the experimental data. It has been proved that very low values of r would cause significant deviation for the saturation condition, while vary high values might cause convergence problem (Liu *et al.*, 2012). In this study, the values of both r_l and r_v are considered to be 5500 s^{-1} for all simulation cases. This value was acquired based on a trial and error procedure. Moreover, by using this value the differences between the interface temperature and saturation temperature are observed to be less than 0.9 °C. The corresponding condensation source term in the energy equation can be calculated as:

$$S_E = -S_l h_{lv} \tag{15}$$

where h_{lv} is the latent heat of condensation. The source terms due to the condensation phenomenon in the mass and energy equations are incorporated into the ANSYS FLUENT 17.1 software via a 'user defined function'.

Furthermore, the average condensation heat transfer coefficient is calculated as follows:

$$h_{ave} = \frac{q''}{T_{sat} - T_{wall,ave}} \tag{16}$$

where q'' and $T_{wall,ave}$ are the heat flux and average tube wall temperature, respectively. In a previous experimental study, the average tube wall temperature was taken as the arithmetic average of thermocouples along the tube of Meyer *et al.* (2014) and Adelaja *et al.* (2017). In the present numerical simulations, the average tube wall temperature is calculated by the ANSYS FLUENT 17.1 commercial software package after achieving the convergence criterion. Furthermore, the pressure drops in the present study are the sum of the frictional, momentum, and static pressure drops, that are automatically calculated by the solver.

The following assumptions are considered for the simulations:

1. The experimental observations show that the flow regimes are stratified, stratified-wavy, annular or churn. Therefore, it is feasible to capture the liquid-vapour interface by the VOF method.
2. It is assumed that the flow field is unsteady, turbulent, and three-dimensional.

3. Single velocity and temperature values are shared by the liquid and vapour phase in each computational cell.
4. As the temperature variations are very small, the properties of the liquid and vapour phases are assumed to be constant under the specified operating conditions.
5. The contact angle between the fluid and tube wall is set at 5.8° (Vadgama and Harris, 2007). This angle is used to adjust the surface normal in cells near the wall. This boundary condition results in the adjustment of the curvature of the surface near the wall, and becomes critical when the fluid in contact with the wall is moving relative to the wall (Brackbill *et al.*, 1992). If ω_w is the contact angle at the wall, then the surface normal at the live cell next to the wall is calculated as (Brackbill *et al.*, 1992):

$$\hat{n} = \hat{n}_w \cos\omega_w + \hat{t}_w \sin\omega_w \tag{17}$$

where $\hat{n}_w$ and $\hat{t}_w$ are the unit vectors normal and tangential to the wall, respectively. The combination of this contact angle, with the normally calculated surface normal one cell away from the wall, determines the local curvature of the surface, and this curvature is used to adjust the body force term in the surface tension calculation.
6. As the initial condition, the tube is considered to be filled by the vapour phase, with a constant temperature equal to the saturation temperature.

The above-mentioned governing equations is solved using the ANSYS FLUENT 17.1 commercial software package. The Simple algorithm is also applied to attain the pressure-velocity coupling. To attain a stable solution procedure, all convective fluxes are approximated using a second-order upwind method, whereas the diffusive fluxes are discretised by central differencing. The Geo-Reconstruct scheme is also utilised in order to capture the proper liquid-

vapour interphase. In addition, the convergence criterion is set to 10^{-5} for the all residuals, and a time-step size of 10^{-4} s is used for all simulation cases. Moreover, all the presented results are for t = 60 s, in which the above convergence criterion is achieved.

3. Experimental database

In this study, the numerical results are validated by the experimental data of Meyer *et al.* (2014) and Adelaja *et al.* (2017) for the condensation heat transfer coefficient and pressure drop, respectively, and the captured flow regimes are compared with the photographs of the experimental study by Lips and Meyer (2012b).

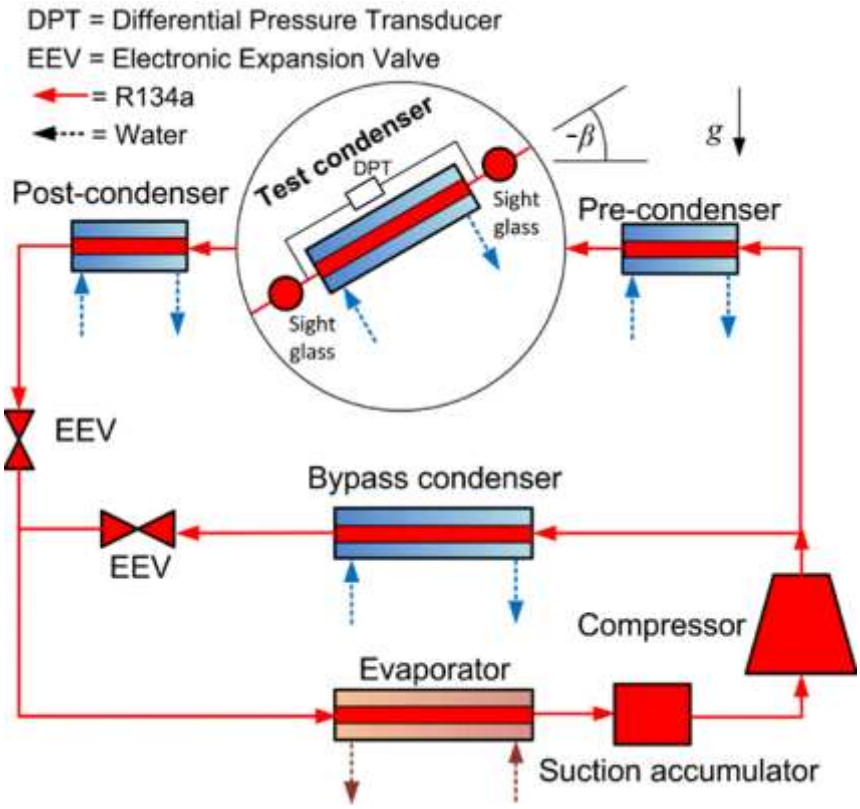

Figure 1. Experimental set-up (Meyer *et al.*, 2014).

The experimental setup is depicted in Figure 1. The setup comprises of a main vapour compression cycle for the refrigerant R134a and several water loops to service the condensers and the evaporator. The cooling capacity of the experimental setup is approximated to be 10 kW. The test section comprises an annulus counter-flow heat exchanger, in which water flows in the annulus, and the refrigerant flows through the test section. Therefore, condensation occurs in the inner tube. The diameter and length of the inner tube test section are 8.38 mm and 1488 mm, respectively. To record the flow regimes the outlet of the tube is filmed with a video camera aligned with a sight glass tube with an internal diameter approximately equal to that of the test section tube. The predicted flow regimes are also captured at this section of the tube for comparative purposes. During the experiments, the condensation heat transfer rate is maintained at 250 W (giving an average of 5050 W/m^2 on the tube surface) by regulating the water mass flow rate and temperature, through the annulus. Therefore, a uniform heat flux of 5050 W/m^2 is set as a boundary condition on the tube surface. Although the heat flux is not constant during the experiments, its variations are not considerable as the tube length is relatively short (Adelaja *et al.*, 2017; Lips and Meyer, 2012b; Meyer *et al.*, 2014). Pressure drops along the tube are measured by pressure gauges at the inlet and outlet regions of the tube. The uncertainties of the average heat transfer coefficient and pressure drop are ± 10% and 100 Pa, respectively. More details concerning the experimental apparatus can be found in Adelaja *et al.* (2017).

Table 1 presents the operating conditions of the current numerical simulations, according to the available experimental data of (Adelaja *et al.*, 2017; Lips and Meyer, 2012b; Meyer *et al.*, 2014).

Table 1. Simulation operating conditions

Parameter	Range
G [kg/m^{2}s]	100 – 400
x_m [-]	0.1 – 0.9
T_{sat} [°C]	30 – 50
β [°]	-90 – +90

4. Results and discussion

4.1. Validation of numerical method

Figure 2 shows the effect of grid size on the condensation heat transfer coefficient and pressure drop along the tube. The test cases for the condensation heat transfer coefficient (Figure 2 (a)) and pressure drop (Figure 2 (b)) are G = 200 kg/m^{2}s, T_{sat} = 50 °C, and x_m = 0.5, and G = 100 kg/m^{2}s, T_{sat} = 30 °C, and x_m = 0.25 (average of vapour qualities between the inlet and outlet regions of the tube). Three grid sizes, with 640 000, 960 000 and 1 680 000 quadrilateral cells, were studied. In general, the results for each grid size exhibit adequate consistency with the experimental data of Meyer *et al.* (2014) and Adelaja *et al.* (2017); however, it is concluded that the results for grid sizes greater than 960 000 cells change by less than 4%. Therefore, the grid with 960 000 cells is used for all the simulations in this study.

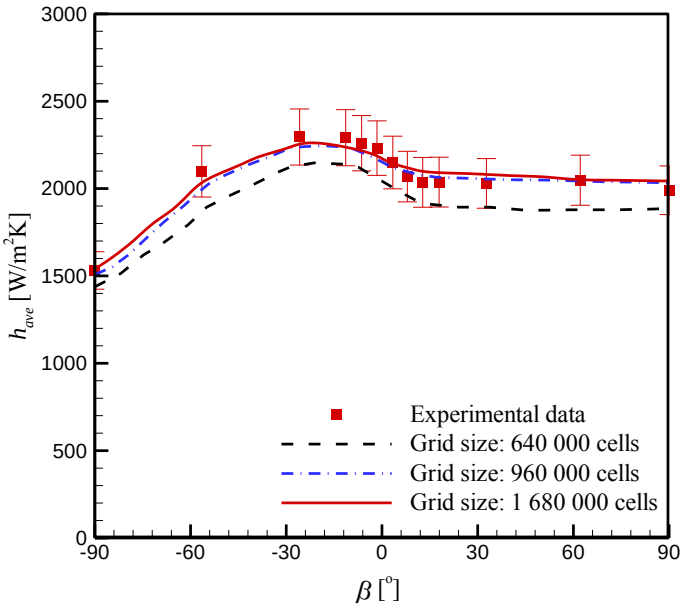

G = 200 kg/m^{2}s, T_{sat} = 50 °C and x_m = 0.5

(a)

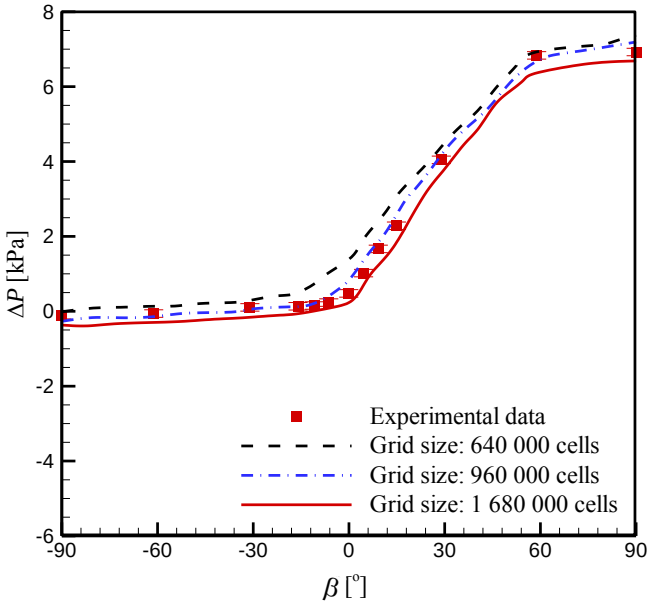

G = 100 kg/m^{2}s, T_{sat} = 30 °C and x_m = 0.25

(b)

Figure 2. Effect of grid size: (a) condensation heat transfer coefficient, and (b) pressure drop along tube.

Table 2. Results of GCI study for: (a) condensation heat transfer coefficient, and (b) pressure drop. (a) Condensation heat transfer coefficient

β [°]	$h_{ave,1}$ [W/m^{2}K]	$h_{ave,2}$ [W/m^{2}K]	$h_{ave,3}$ [W/m^{2}K]	GCI_{12}	GCI_{23}	$\frac{GCI_{23}}{s^e GCI_{12}}$
-90	1490.000	1506.665	1540.441	0.014	0.027	0.989
-60	1880.000	1903.580	1974.265	0.008	0.023	0.988
-30	2191.000	2231.160	2236.618	0.027	0.004	0.982
0	2138.000	2149.355	2154.412	0.012	0.005	0.995
30	2040.000	2059.448	2084.559	0.041	0.052	0.991
60	2033.000	2048.117	2051.471	0.012	0.003	0.993
90	2000.000	2034.490	2044.118	0.030	0.008	0.983

(b) Pressure drop

β [°]	Δp_1 [kPa]	Δp_2 [kPa]	Δp_3 [kPa]	GCI_{12}	GCI_{23}	$\frac{GCI_{23}}{s^e GCI_{12}}$
-90	0.250	-0.240	-0.367	3.306	0.892	1.042
-60	0.133	-0.133	-0.282	5.677	3.165	0.997
-30	0.062	0.060	-0.173	0.000	0.041	1.033
0	0.970	0.927	0.299	0.004	0.062	1.046
30	4.600	4.450	3.825	0.013	0.055	1.034
60	6.956	6.732	6.353	0.058	0.102	1.033
90	7.373	7.193	6.687	0.017	0.048	1.025

Apart from the study of the effect of grid size on the condensation heat transfer coefficient and pressure drop along the tube, a grid convergence index (GCI), method (Roache, 1998) is used to ensure that the calculated solutions are within the asymptotic range. Table 2 presents the results of the GCI. In Table 2, GCI, s, and e are the grid convergence index, effective grid refinement ratio, and order of convergence, respectively. The indices 1, 2, and 3 represent the grid sizes of 640 000, 960 000, and 1680 000, respectively. The results of the GCI provide further confirmation that the grid size with 960 000 quadrilateral cells can be used for the simulations in present work, as the ratio $\frac{GCI_{23}}{s^e GCI_{12}}$ is close to unity, indicating that the calculated

solutions are within the asymptotic range (Roache, 1998). Details of the calculation procedure can be found in (Roache, 1998).

4.2. Flow regimes

Figures 3 and 4 show the contours of volume fractions at two conditions: G = 100 kg/m^{2}s, T_{sat} = 40 °C, and x_m = 0.25 (Figure 3), and G = 200 kg/m^{2}s, T_{sat} = 40 °C, and x_m = 0.5 (Figure 4). In both figures, the volume fractions at seven inclination angles, from vertically downwards (β = -90°), to vertically upwards flow (β = 90°), are presented, and blue and red colours represent the volume fraction of the vapour and liquid phases, respectively.

The graphical data from the numerical simulations, and the photographs of the experiment, are at the outlet of the test section. The numerical images are taken over a period of t = 60 s, during which time the variations of all parameters was less than 3%. This was in good agreement with previous experiments (Lips and Meyer, 2012b).

In general, a good agreement between the predicted and the observed flow regimes can be observed. Although there are differences between the numerical and experimental images, the captured flow regimes are correct. Moreover, it is worth mentioning that the numerical solver can capture the changes in flow regime at different inclination angles that means that the appropriate governing equations, as well as inter-phase mass momentum and energy source terms, are utilised.

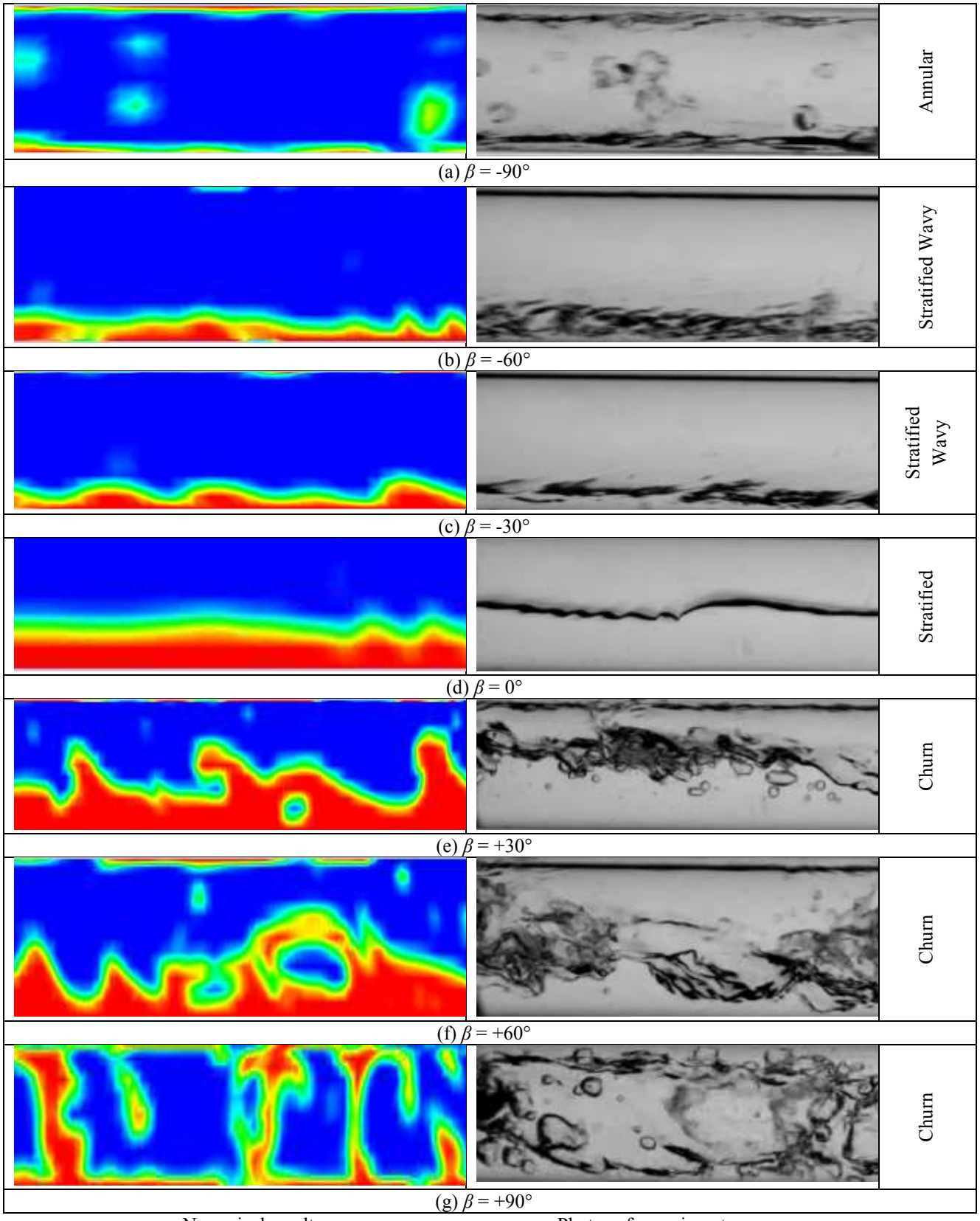

Figure 3. Volume fraction contours and experimental data of Lips and Meyer (2012b) at x_m = 0.25, G = 100 kg/m^{2}s, T_{sat} = 40 °C, and inclination angles: (a) β = -90°, (b) β = -60°, (c) β = -30°, (d) β = 0°, (e) β = 30°, (f) β = 60°, and (g) β = 90°.

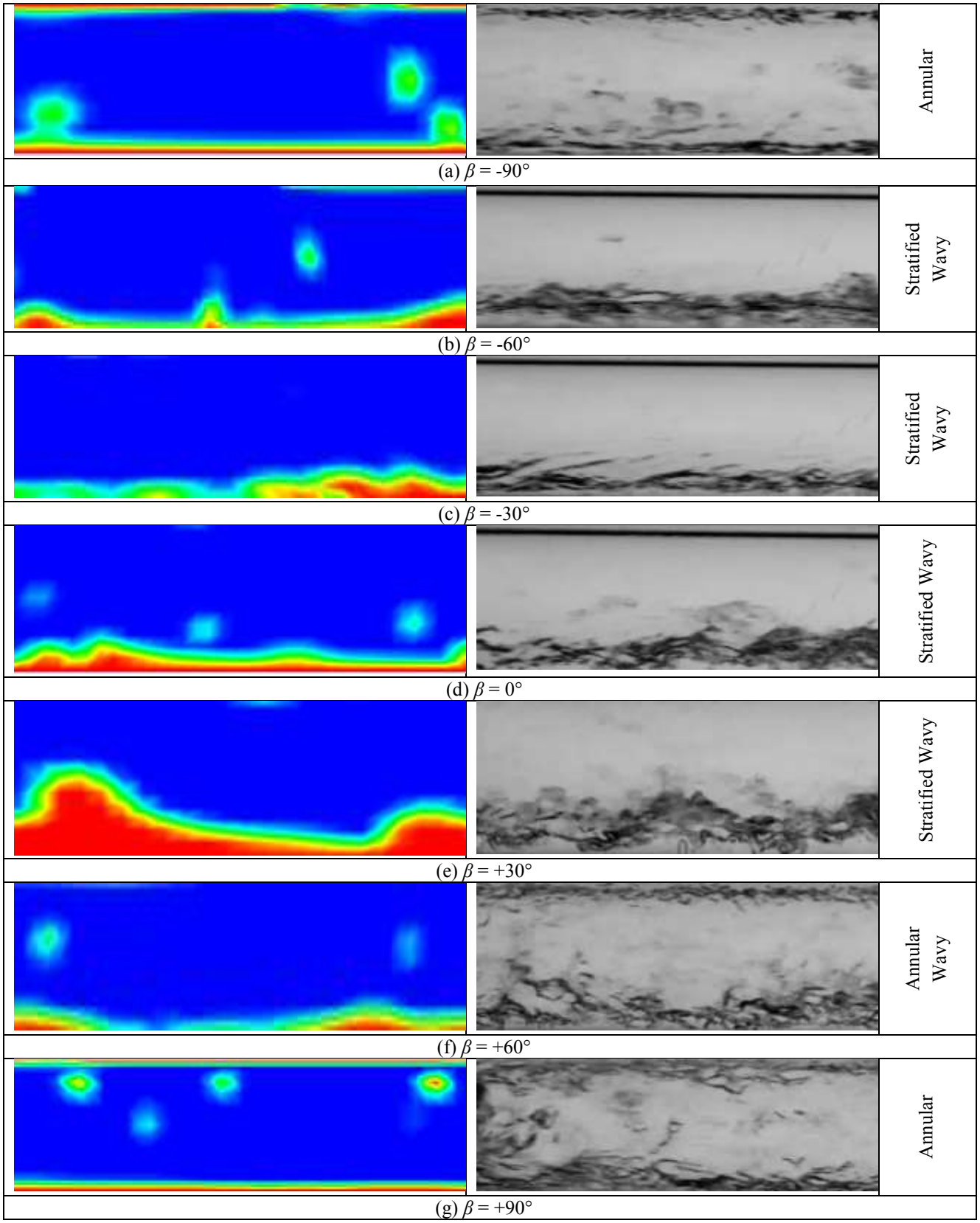

Figure 4. Volume fraction contours and experimental data of Lips and Meyer (2012b) at $x_m = 0.5$, $G = 200$ kg/m^{2}s, $T_{sat} = 40$ °C, and inclination angles: (a) $\beta = -90°$, (b) $\beta = -60°$, (c) $\beta = -30°$, (d) $\beta = 0°$, (e) $\beta = 30°$, (f) $\beta = 60°$, and (g) $\beta = 90°$.

At low mass fluxes and qualities, when the flow inclination angle changes upwards from horizontal ($\beta > 0°$), the flow regime changes from annular, or stratified-wavy, to churn, as shown in Figure 3. In Figure 3 (a), the flow regime is annular when the flow direction is vertically downwards ($\beta = -90°$). In Figures 3 (b)–(d), the flow regimes are stratified, or stratified wavy, when the downwards inclination angle β increased from -60° to 0°. This is due fact that the gravitational force causes the liquid phase that is the heavier phase, to accumulate on the bottom of the tube. When the flow direction changes to upwards, the direction of the gravity force is opposite to the flow, and causes some instabilities on the liquid film on the bottom of the tube. As a result, the flow regime changes to churn (Figures 3 (e)–(g)) for upward flows with inclination angles $\beta > 0°$.

In Figure 4, in which the results for $G = 200$ kg/m^{2}s, $T_{sat} = 40$ °C, and $x_m = 0.5$ are presented, the flow regimes for the vertically downwards flow ($\beta = -90°$) and vertically upwards flow ($\beta = 90°$), are annular, while all the other flow regimes, $-60° < \beta < 60°$, are stratified wavy. Therefore, as no changes in the flow regimes occur within this range of inclination angles, the pressure drops and condensation heat transfer coefficients also do not change considerably within this range, as was reported in the experimental work of Lips and Meyer (2012b). This interpretation will be used in the subsequent sections to discuss the effect of the inclination angle on the heat transfer coefficient and pressure. Further explanation and simulations cases on the flow regimes at different qualities, mass fluxes, and inclination angles can be found in (Abadi *et al.*, 2018a; Abadi *et al.*, 2018b).

Figure 5(a) shows the simulated flooded angle and liquid hold-up for $G = 100$ kg/m^{2}s, and $T_{sat} = 40$ °C, and three different vapour qualities. The flooded angle and liquid hold-up are defined as the total angle of the tube that is covered by the liquid phase, and the ratio of liquid film

thickness at the bottom of the tube to the tube diameter, respectively. The presented tube inclination angle varies from β = -90° to β = 30°, because for cases of β > 30°, the flow regimes are churn flow, and, as a result, a clear liquid-vapour interface cannot be observed.

The liquid hold-up increases smoothly for downwards tube inclinations due to a decrease in the gravity-assisted force in the flow direction. The minimum value of liquid hold-up occurs at β = -90°, at which point the flow regime is annular. The liquid hold-up increases significantly in the upwards flow direction as a result of the opposing gravity force. It can also be seen in Figure 5 that the flooded angle is a maximum at β = -90°, where the flow regime is annular. By increasing the inclination angle to the region -45° < β < -30°, the flooded angle becomes a minimum. In this region, the condensation heat transfer coefficient reaches a maximum, as the vapour phase has the greatest direct contact area with the tube surface. With a further positive increase of the inclination angle, the flooded angle increases due to the effect of the gravity force, and the change of flow regime from stratified flow to churn flow. As expected, with the increase in the mean vapour quality, both the flooded angle and liquid hold-up decreased.

In Figure 5(b), a similar plots are presented for different saturation temperatures and inclination angles for G = 100 kg/m^{2}s and x_m = 0.5. The results for the liquid hold-up clearly show that the increase of the saturation temperature leads to an increase of liquid film thickness. It can be attributed to the fact that the condensation heat transfer coefficient decreases with the increase of the saturation temperature. Such interpenetration is valid for all inclination angles. The acquired results are used for justification of the changes in the condensation heat transfer coefficients in sec. 4.3.

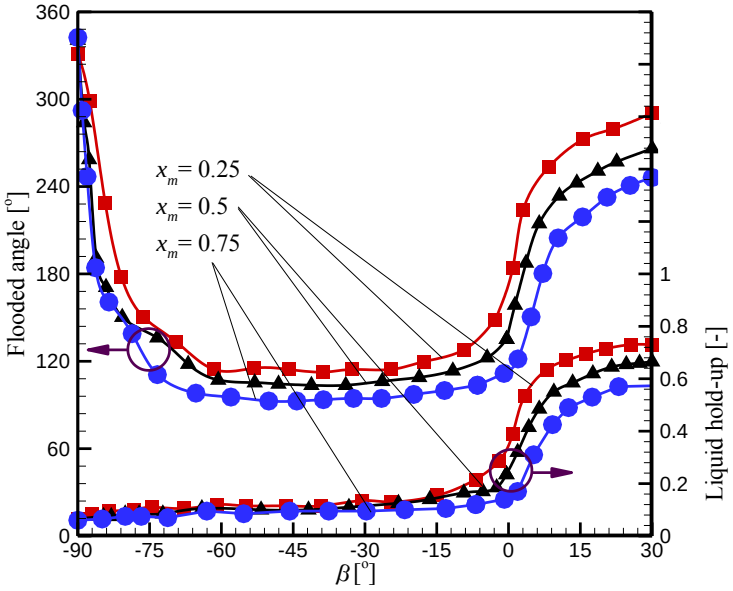

(a)

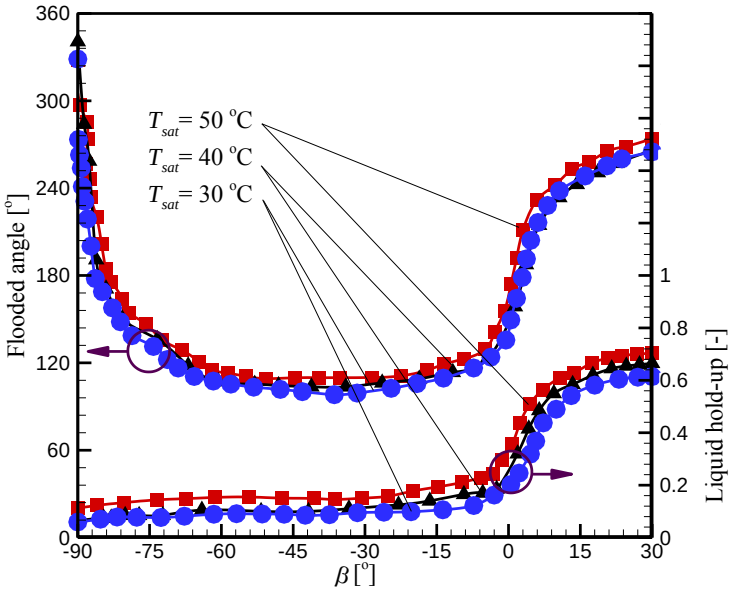

(b)

Figure 5. Liquid hold-up and flooded angle as function of tube inclination angle at G = 100 kg/m^{2}s and T_{sat} = 40 °C.

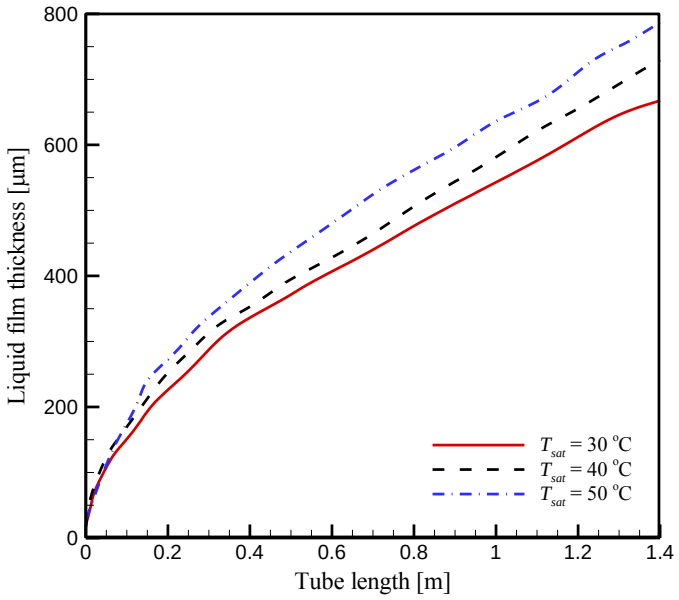

Figure 6. Evolution of liquid film thickness along the tube length at different saturation temperatures for x_m = 0.75, G = 300 kg/m^{2}s and β = -90°.

Figure 6 shows the evolution of the liquid film thickness along the tube length at different saturation temperatures for x_m = 0.75, G = 300 kg/m^{2}s and β = -90°. The flow regime for all cases in this figure is annular, therefore there is no circumferential variations in the liquid film thickness. Apparently, there is a sharp increase in the liquid film thickness at the entrance region due to the high condensation heat transfer coefficient. Because at this region the vapour phase is in direct contact with the tube wall. It should be noticed that the liquid film thickness is not zero at the tube entrance, as the vapour quality is not unity. The software calculates the volume fraction of the liquid phase as well as the liquid film thickness according to the input vapour quality. The liquid film thickness gradually increase along the tube length due to the condensation phenomena. Furthermore, the liquid film thickness increases with increase of the saturation temperature. It can be attributed to the lower condensation heat transfer coefficient at the higher saturation temperatures.

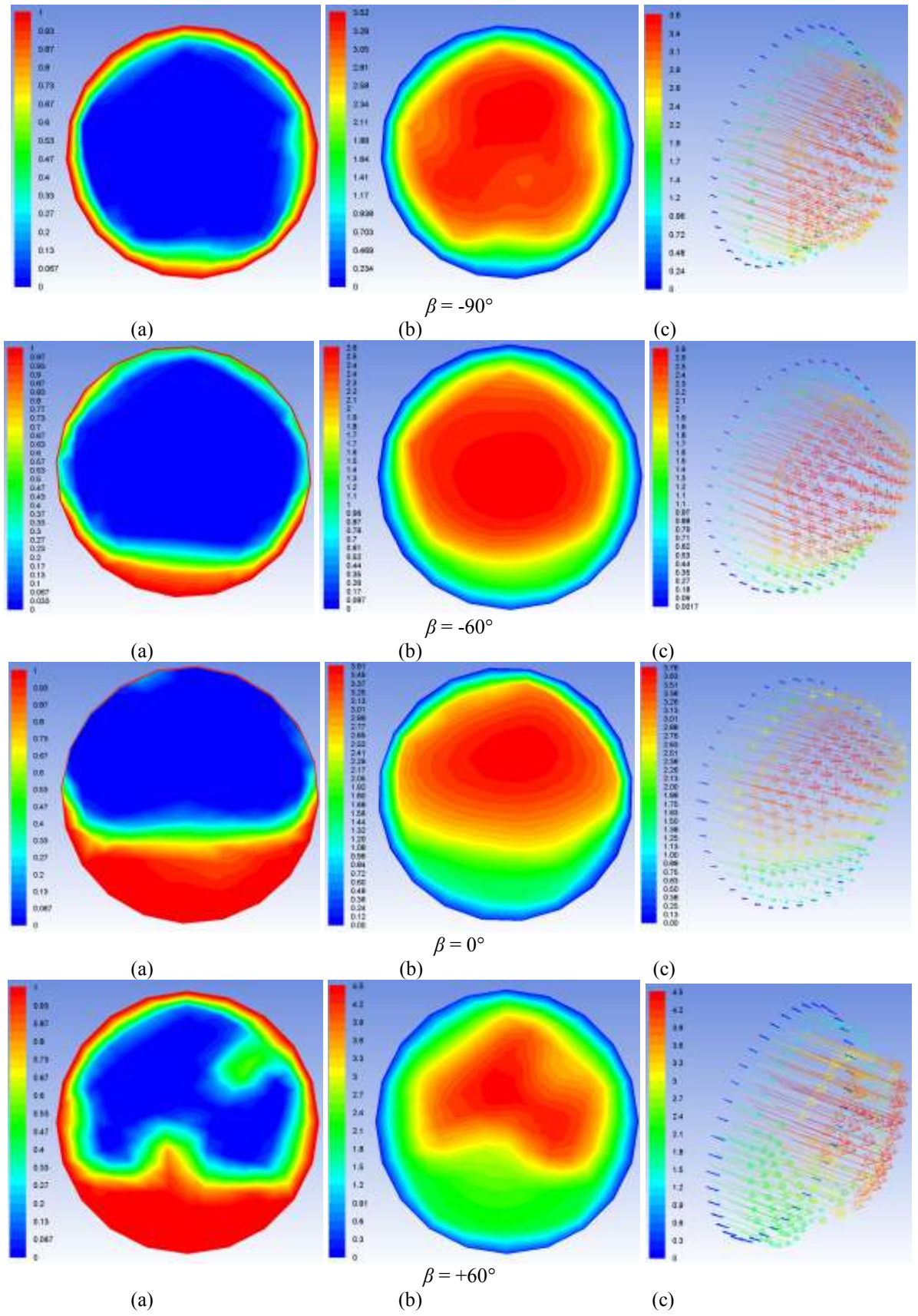

Figure 7. Contours of (a) vapour volume fraction, (b) velocity in m/s, and (c) velocity vectors in m/s for G = 200 kg/m^{2}s, x_m = 0.75, T_{sat} = 40 °C, and different inclination angles.

The contours of the vapour volume fraction, velocity, and velocity vectors at the outlet section of the tube for G = 200 kg/m^{2}s, x_m = 0.75, T_{sat} = 40 °C, and different inclination angles are presented in the Figure 7. At β = -90°, the flow regime is annular and the liquid film covers the tube surface uniformly, which means that there is no contact between the vapour and tube wall. As a result, the thermal resistance is the highest in the annular flow regime, and the lowest condensation heat transfer coefficient may occur. In the annular flow regime, the maximum velocity occurs at the core of the tube and gradually reaches to zero at the tube wall. At β = -60°, the flow regime is annular-wavy, and the more liquid phase accumulates at the bottom of the tube due to gravity compared to the case of β = -90°. Therefore, the liquid film thickness is lower at the top region of the tube surface, which results in higher heat transfer coefficient compared to the annular flow regime. The contour of velocity shows that the maximum velocity occurs at the top region of the tube, where the vapour phase is passing. At β = 0°, the liquid film becomes thicker, because there is more assisting gravity force along the flow direction. Therefore, the condensation heat transfer coefficient is lower compared to the case of β = -60°. The contour of velocity and the corresponding vector are similar to the stratified-wavy flow regime, but the maximum high speed core is smaller. At β = +60°, the gravity force acts on the opposite direction of the flow and causes in increase of liquid film thickness as well as instability and turbulence at interface of the liquid and vapour phases. In this condition, the flow regime is stratified-wavy or churn flow with thick liquid film thickness, which consequently leads to the lower condensation heat transfer coefficient compared to the cases β = -60° and β = 0°.

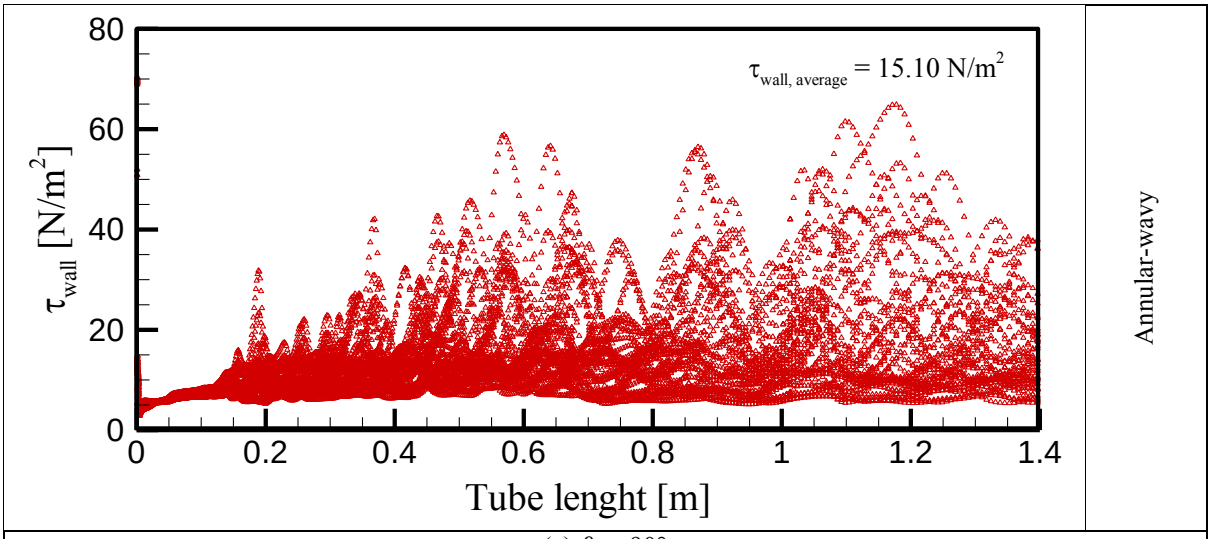

(a) β = -90°

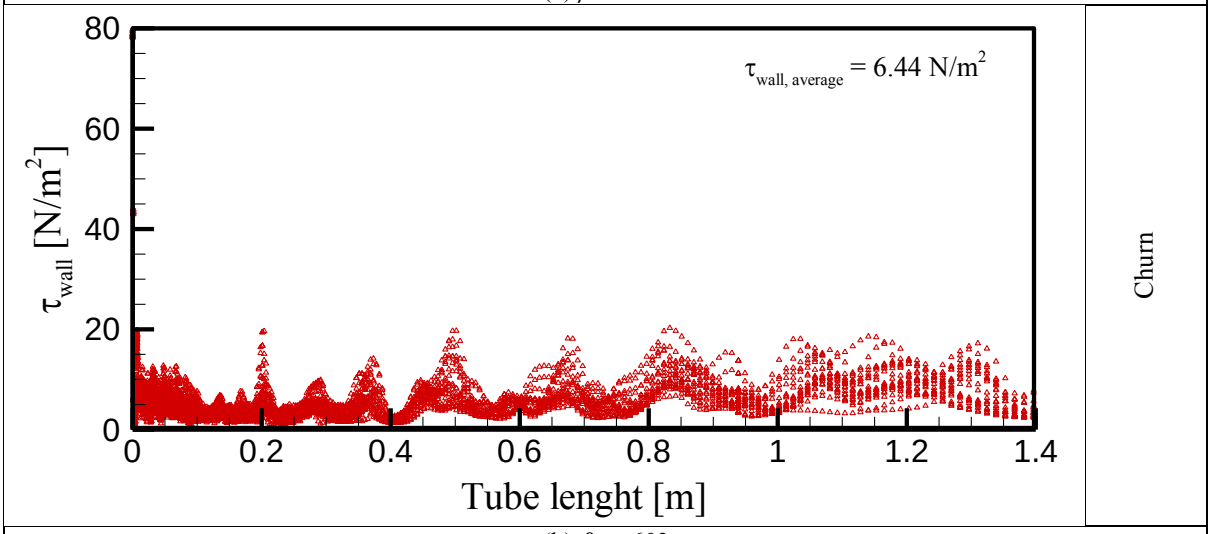

(b) β = -60°

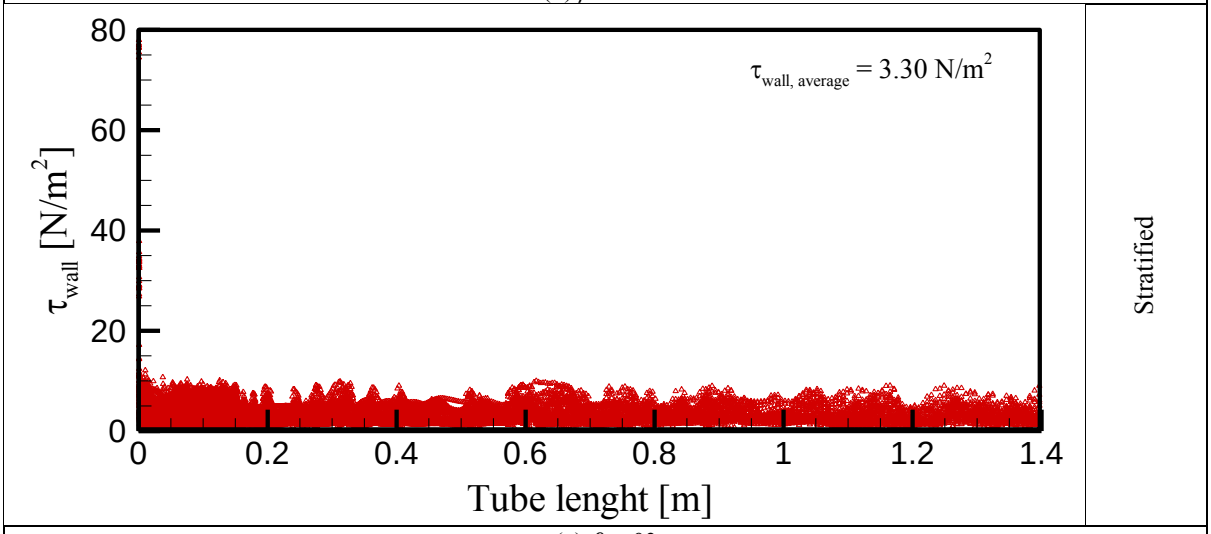

(c) β = 0°

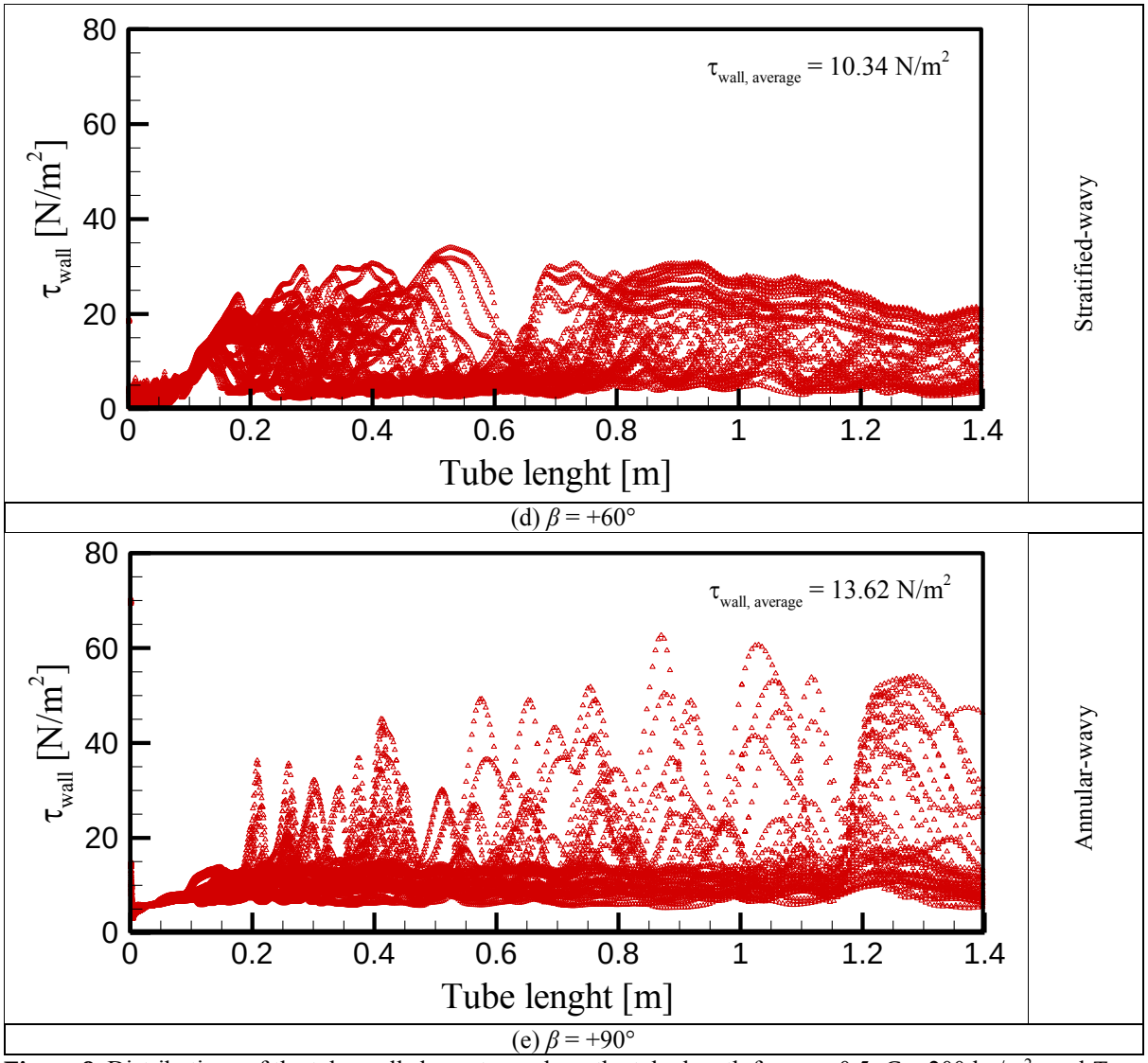

Figure 8. Distributions of the tube wall shear stress along the tube length for x_m = 0.5, G = 200 kg/m^{2}s and T_{sat} = 50 °C: (a) β = +90°, (b) β = +60°, (c) β = 0°, and (d) β = +60°, (e) β = +90°.

Figure 8 depicts the distributions of the wall shear stress along the tube for x_m = 0.5, G = 200 kg/m^{2}s and T_{sat} = 50 °C at different tube inclination angles. The highest average wall shear stresses occurs at β = -90° and β = +90° because in these cases the flow regime is annular and the shear stress is dominant. In the cases β = -90° and β = +90° the wall shear stress is smooth with some abrupt jump corresponds to the waviness of the liquid-vapour interface. In the case β = +60°, in which the flow regime is churn flow, the wall shear stress is not uniform and no specific pattern could be observed. The average wall shear stress is also lower than those for β = -90° and β = +90°. In the case with β = 0°, the flow regime is stratified, as a results the wall

shear stress is uniform along the tube at the lowest average value compared to the other cases. The wall shear stress for β = -60° shows a wavy pattern, as the flow regime is stratified in this condition. Furthermore, the average value in this case is higher than in β = -60°, because for the negative flow direction the gravity force increases the liquid velocity along the tube and consequently higher shear stress.

In this study the ratio of the dominant forces, gravity and shear forces, for some cases are presented using the well-known Wallis dimensionless velocity (Wallis, 1969), j^*_v, which is defined as:

$$j^*_v = j_v \left[\frac{\rho_v}{g \cos(\beta) D(\rho_l - \rho_v)} \right]^{0.5} \tag{18}$$

$$j_v = \frac{Gx}{\rho_v} \tag{19}$$

where j and D are the superficial velocity and tube diameter, respectively. Figure 9 shows the dimensionless velocity for T_{sat} = 50 °C, and different mass fluxes, vapour qualities and tube inclination angles. When the mass flux is G = 100 kg/m^{2}s (Figure 9(a)), the Wallis dimensionless velocities are less than unity for almost all vapour qualities and inclination angles, except for some cases with $\beta \leq$ -75° and $\beta \geq$ +75°. Which means that the gravity force is more dominant than the shear force. As a result, in these cases the flow regimes are not annular. For the cases with $\beta \leq$ -75° and $\beta \geq$ +75° the flow regimes tend to be annular which means that the shear stress is more dominant than the gravity force (the corresponding values are not shown, as they are much higher than 10.0). The results also shows that with an increase of the vapour quality the value of Wallis dimensionless velocity increases, which means that the shear stress strengthens. Furthermore, it can be observed that increasing the tube inclination

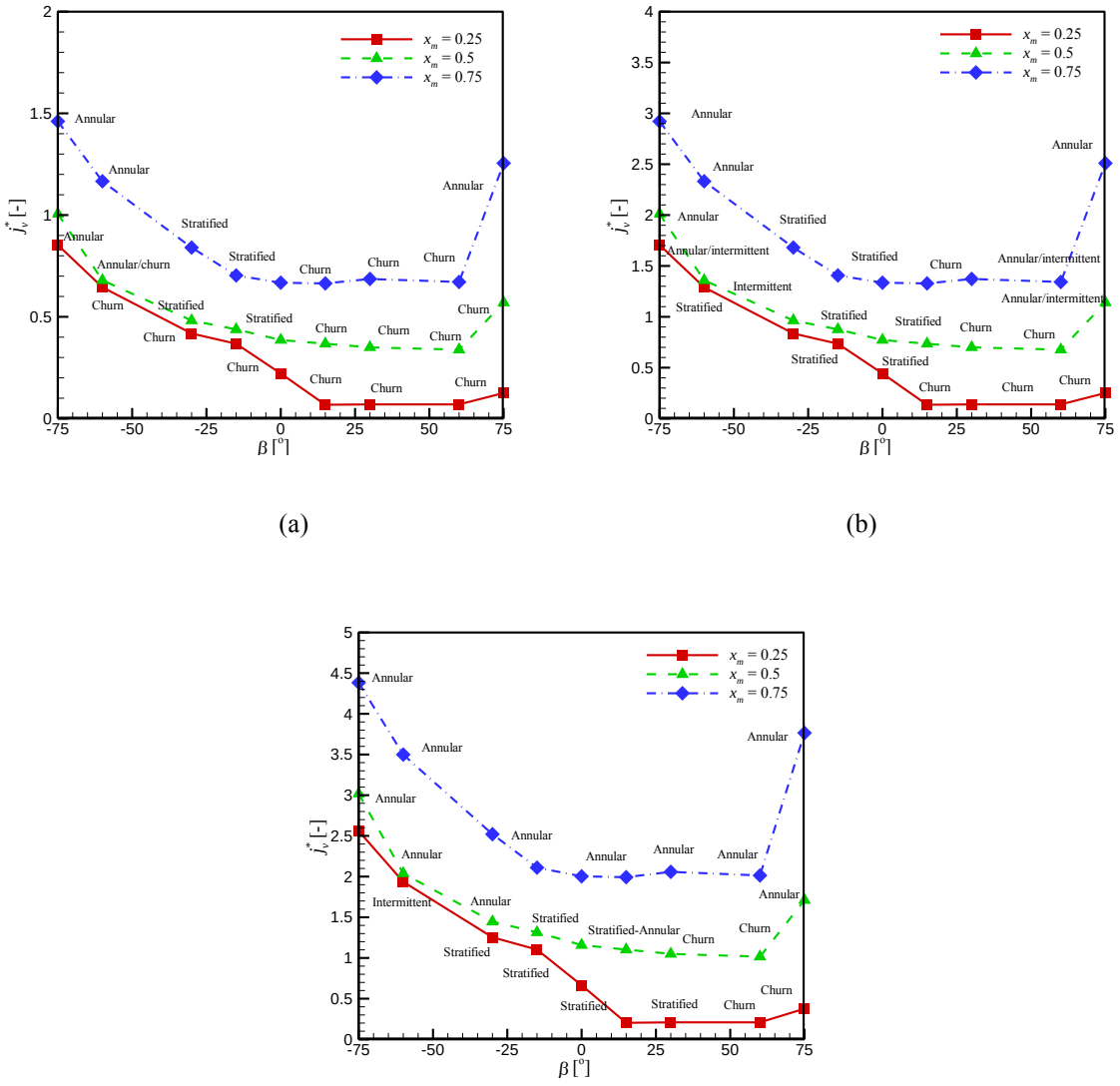

(a) (b)

(c)

Figure 9. Ratio of shear force to gravitational force, j_v^*, for different operating conditions; (a) G = 100 kg/m^{2}s, (b) G = 200 kg/m^{2}s, (c) G = 300 kg/m^{2}s.

angle decreases the Wallis dimensionless velocity, which means that the gravity force is strengthening compared to the shear force. With an increase in the mass flux to G = 200 and 300 kg/m^{2}s (Figure 9(b) and (c) respectively), the Wallis dimensionless velocity increases considerably, therefore it can concluded that the shear stress becomes dominant in higher mass fluxes. As a result the flow regimes tend to annular flow in these operating conditions. It is also

worth mentioning that the predicted flow regimes are compatible with the observed flow patterns in the experimental work of Olivier *et al.* (2016).

4.3. Heat transfer coefficients

The variations of the condensation heat transfer coefficients are strongly dependant on the flow regime and the corresponding liquid film thickness on the tube surface. The former is discussed in detail in sec. 4.2 and the later will be explained below, then the variations of the condensation inside the tube for different operating conditions will be investigated.

In Figure 10 the variations of the thermal resistance along the tube length for T_{sat} = 40 °C, two mass fluxes of G = 100 and 200 kg/m^{2}s, and different vapour qualities and inclination angles. The results show that the thermal resistance increases along the tube. This can be attributed to the fact that the thickness of the liquid film increases along the tube due to condensation. Furthermore, it can be seen that the highest thermal resistance occurs at inclination angles of β = -90° and β = +90°, for which the flow regime is often annular. This can be due to the fact that in the annular flow regime the liquid phase always covers all the tube surface and performs as a barrier toward the heat flux. Therefore is will be expected to have the minimum heat transfer coefficient for the annular flow regime. Another point is that the thermal resistance decreases with the increase of the vapour quality and mass flux, because with increase of the vapour quality and mass flux, the liquid film thickness on the tube surface decreases.

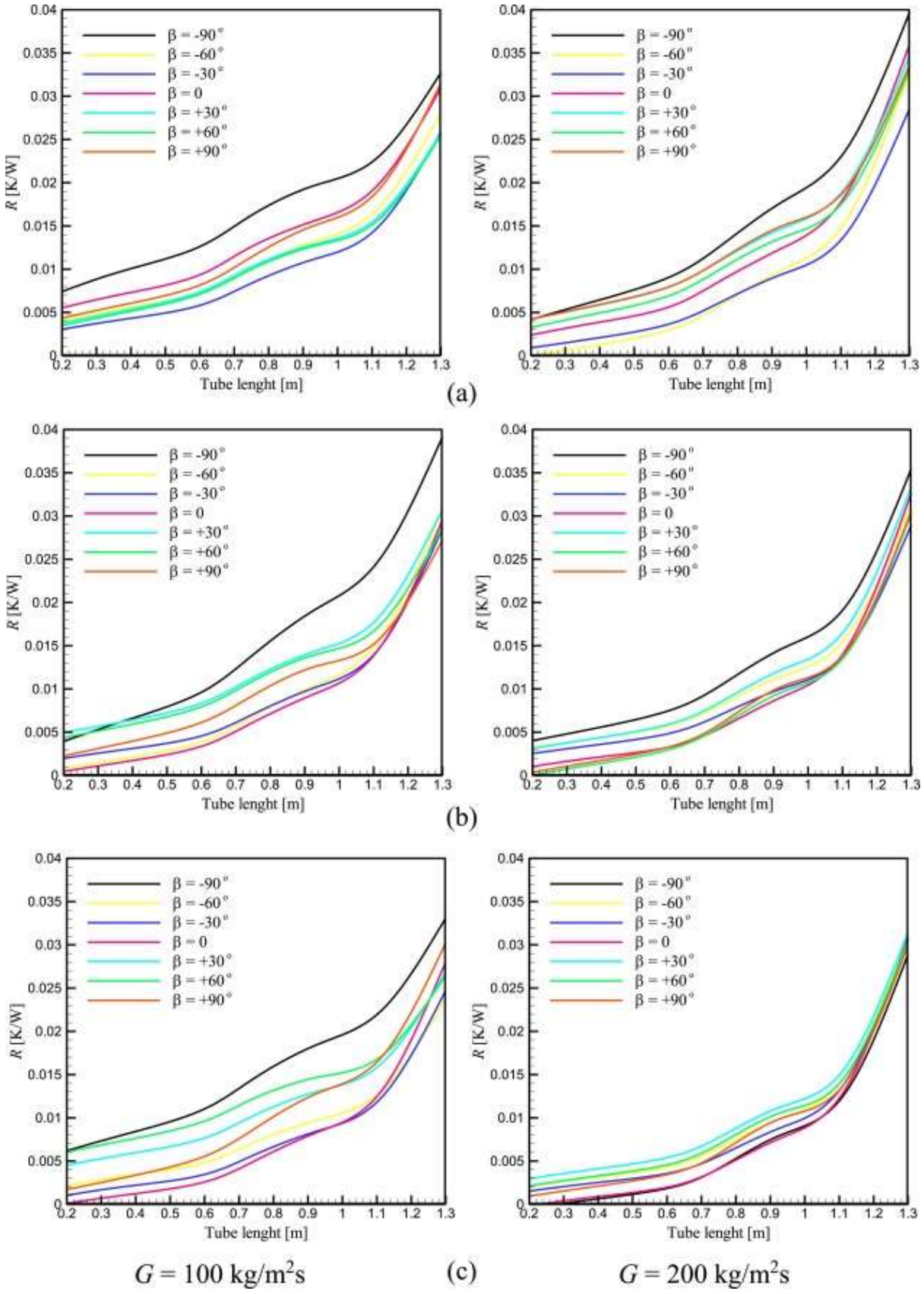

Figure 10. Variations of the thermal resistance along the tube length for different inclination angles and mass fluxes at T_{sat} = 40 °C: (a) x_m = 0.25, (b) x_m = 0.5, and (c) x_m = 0.75.

Figure 11 shows the effect of saturation temperature on the heat transfer coefficient at G = 200 kg/m^{2}s, and different inclination angles and vapour qualities. From these results it can be seen that the proposed numerical method can satisfactorily predict the experimental condensation heat transfer coefficient inside an inclined smooth tube. The maximum difference between the numerical study, and the experimental data of Meyer *et al.* (2014), is 8%. The results also show that the condensation heat transfer coefficient decreases with increasing saturation temperature. This trend can be observed for each vapour quality and tube inclination angle. Two reasons can be stated for this increase. The first reason is that the thermal conductivity of the liquid and vapour phases decreases with increasing saturation temperature, which results in increased thermal resistance during condensation. The second reason is that the vapour density increases with the increase of the saturation temperature and causes a decrease in the vapour velocity as well as momentum exchange between the vapour and liquid phases at the same mass flux, which consequently leads to the decrease in the condensation heat transfer coefficient. The first reason is dominant at lower mass fluxes (Yan and Lin, 1999), while at higher mass fluxes the second reason becomes more important (Jung *et al.*, 2004).

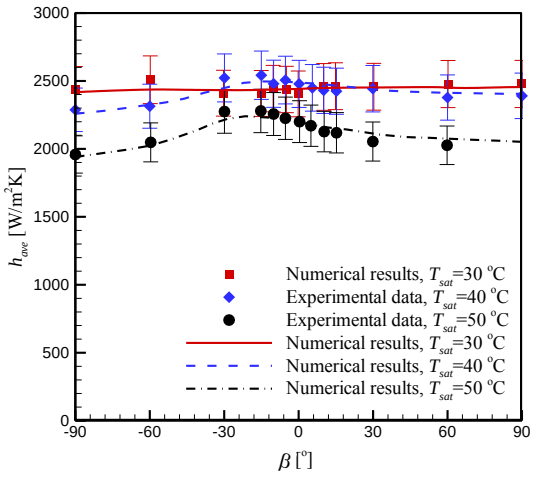

(c)

Figure 11. Effect of saturation temperature on condensation heat transfer coefficient at G = 200 kg/m^{2}s, and different inclination angles: (a) x_m = 0.25, (b) x_m = 0.5, and (c) x_m = 0.75.

It can be seen from the results that, for different tube inclination angles, the condensation heat transfer coefficient increases with tube orientation from β = -90° to β = -30°; decreases from β = -30° to β = 0°; and, becomes approximately constant for positive tube inclination angles. The changes in heat transfer coefficient with respect to the inclination angle can be discussed based on two factors, liquid film thickness and flow regime; these were discussed in the previous section. When β = -90°, the flow regime is annular and the liquid film covers the tube surface completely, resulting in increased thermal resistance, and, consequently, a smaller condensation heat transfer coefficient. When the tube inclination angle changes from β = -90° to β = -30°, the flow regime changes to stratified, or stratified-wavy. Therefore, the liquid film covers only the bottom half of the tube surface, resulting in direct contact between the tube wall and the vapour phase, and, consequently, a greater condensation heat transfer coefficient. When the inclination angle is β = 0°, the effect of the assisting gravitational force gradually dissipates and the liquid film thickness increases consequently, resulting in a smaller heat transfer coefficient. The flow regime at positive inclination angles is typically churn or intermittent; therefore, there is no clear liquid film thickness on the tube surface. As a result, the inclination angle does not have a significant effect on the heat transfer coefficient.

Figure 12 shows the effect of mass flux on the heat transfer coefficient at T_{sat} = 40 °C, and different inclination angles and vapour qualities. It can be seen that the predicted numerical results are in good agreement with the experimental data of Meyer *et al.* (2014). Moreover, as was predicted, the condensation heat transfer coefficient increases with increasing mass flux, and the effect of the tube inclination angle on the condensation heat transfer coefficient decreases with increasing mass flux. It can be attributed to the fact that at higher mass fluxes the flow regimes are annular flow.

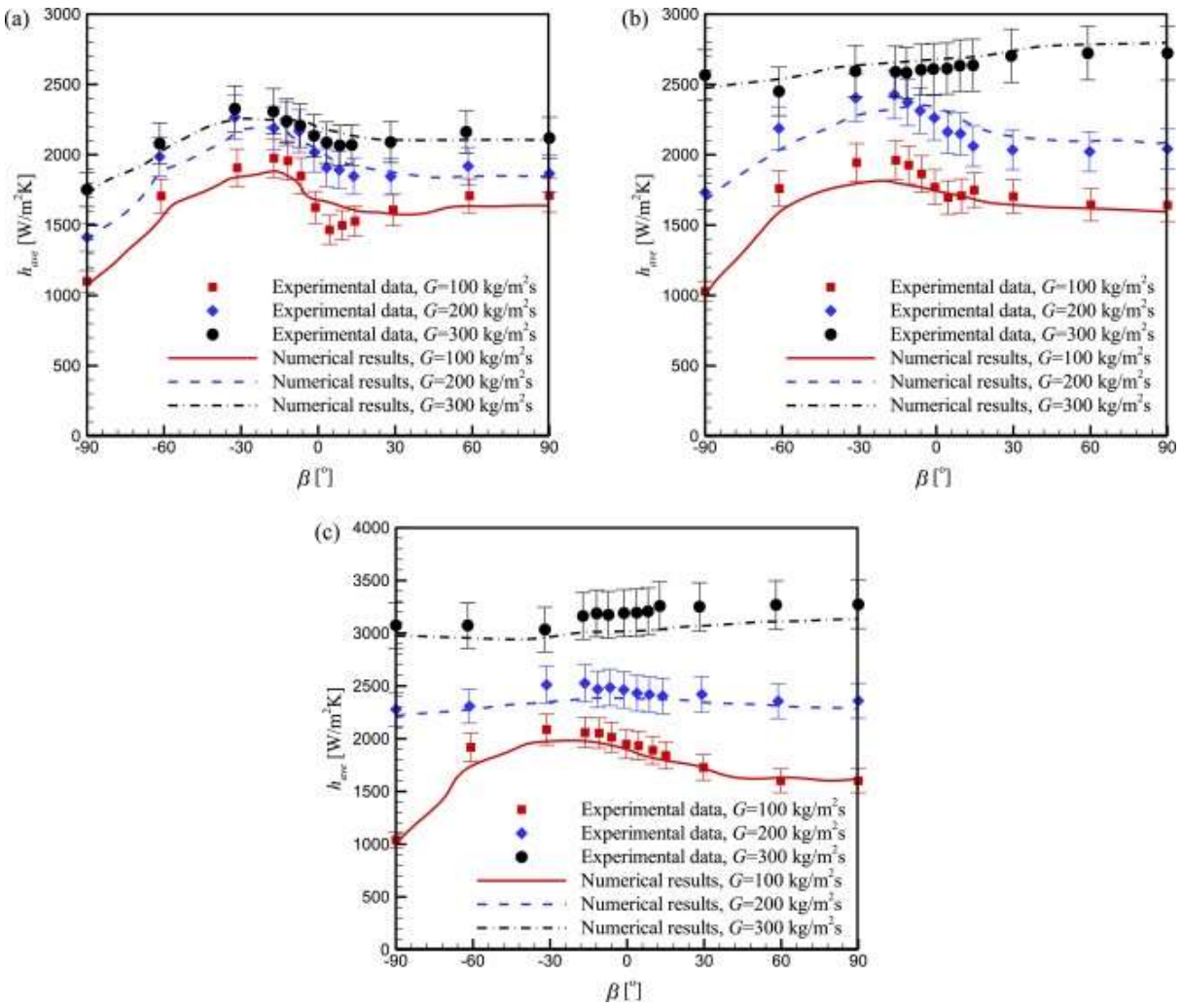

Figure 12. Effect of mass flux on heat transfer coefficient at T_{sat} = 40 °C and different inclination angles: (a) x_m = 0.25, (b) x_m = 0.5, and (c) x_m = 0.75.

The results for T_{sat} = 40 °C, G = 300 kg/m^{2}s, and different inclination angles, with respect to the effect of vapour quality on the condensation heat transfer coefficient, are shown in Figure 13. It can be seen that the effect of the tube inclination angle on the heat transfer coefficient decreases with increasing vapour quality; as with higher vapour quality, the flow regime is approximately annular, where the effect of the shear stress force is greater than that of the gravitational force.

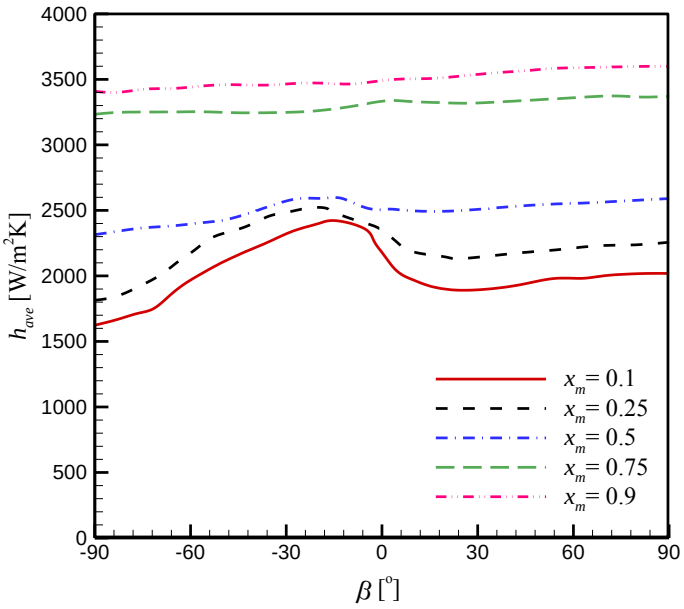

Figure 13. Effect of mean vapour quality on condensation heat transfer coefficient at T_{sat} = 40 °C, G = 300 kg/m^{2}s, and different inclination angles.

In Figures 11-13, the condensation heat transfer coefficients for the lower mass fluxes and vapour qualities show an optimum region between β = -30° to β = -15° depending on the operating condition. This maximum can be attributed to the fact that at this region the flow regime is stratified or stratified wavy and the gravity force enhances the convection effect in the liquid film. An interesting point is that the increase in the condensation heat transfer coefficient occurred by just imposing an appropriate inclination angle and without any additional cost. Therefore this region can be noticed as a suitable design feature for designing the two-phase heat exchangers.

The variations of the local condensation heat transfer coefficients for G = 200 kg/m^{2}s, x_m = 0.25, T_{sat} = 30 °C are presented in Figure 14. The circumferential angle, θ, varies from 0°, at the bottom of the tube, to 180° at the top of the tube. At β = -60°, the liquid film fills the bottom part of tube up to θ = 30°, as a result the corresponding condensation heat transfer coefficient

is low in this region of the tube. At the upper part of the tube, 30° < θ < 180°, the liquid film decreases gradually and in some points the tube surface is in direct contact of the vapour phase, therefore the condensation heat transfer coefficient increases considerably for θ > 30°, and stabilises at an approximately constant value. When the inclination angle changes to β = 0, the liquid film thickness as well as the flooded angle increase, and cause a decrease in the condensation heat transfer coefficient compared to the case with β = -60°. The rapid increase of the condensation heat transfer coefficient occurs at θ = 45° for this case, as the liquid hold-up spans to this point. With a further increase of the tube inclination angle to β = 60°, the flow regime becomes churn flow, that causes a decrease in the condensation heat transfer coefficient. This can be attributed to the fact that in the churn flow regime the liquid phase sporadically hits the tube wall and deteriorates the liquid film on the tube surface, which consequently causes an increase in the thermal resistance.

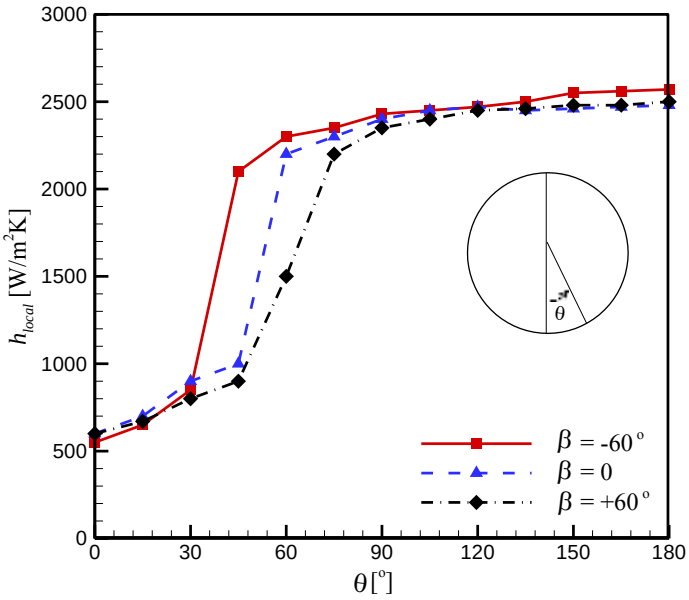

Figure 14. Circumferential distributions of the condensation heat transfer coefficient for G = 200 kg/m^{2}s, xm = 0.25, T_{sat} = 30 °C, and different inclination angles.

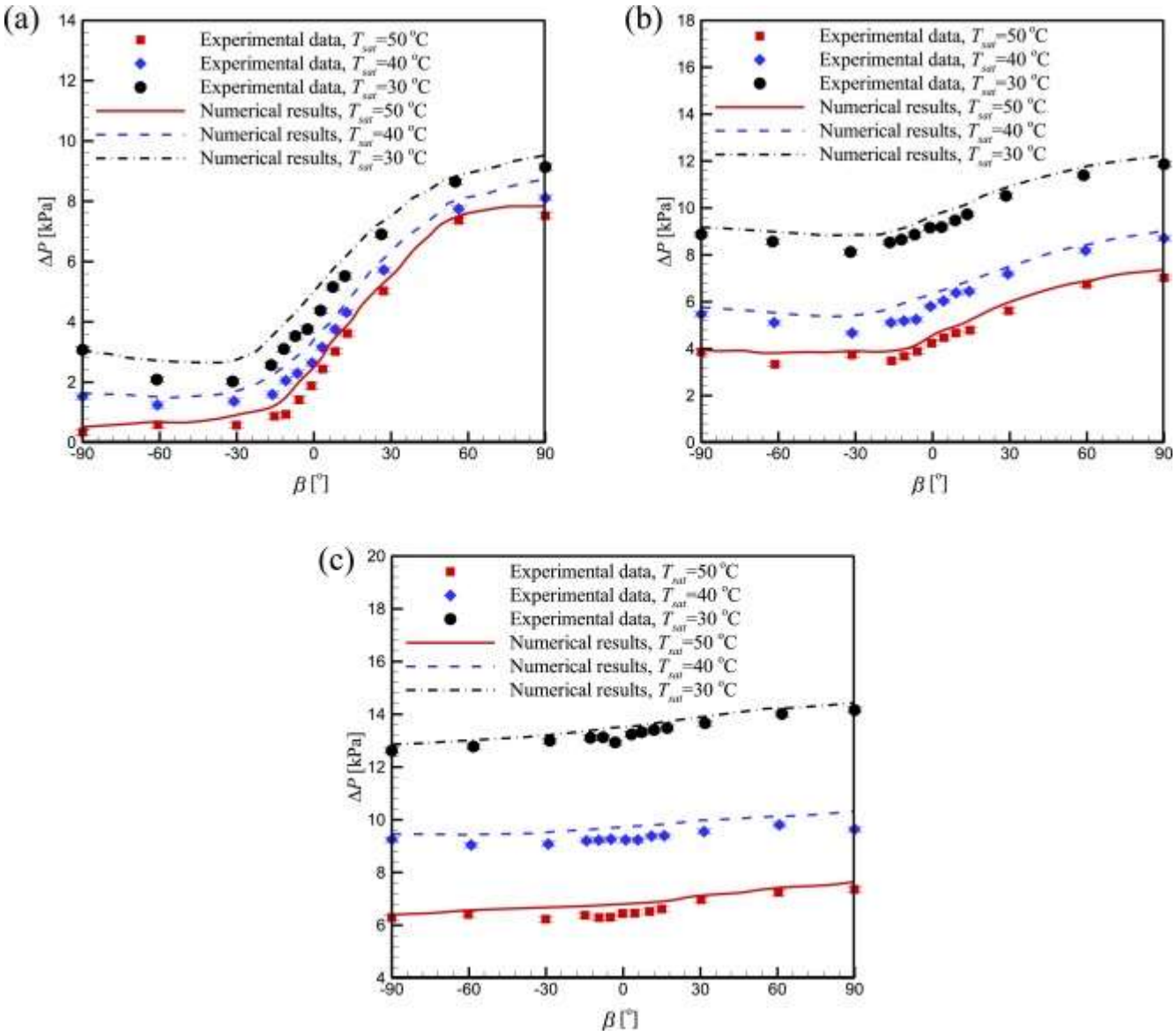

(c)

Figure 15. Effect of saturation temperature on pressure drop along tube at G = 400 kg/m^{2}s, and different inclination angles: (a) x_m = 0.25, (b) x_m = 0.5, and (c) x_m = 0.75.

4.4. Pressure drops

4.4.1. Total pressure drop

Figure 15 compares the numerical results of the pressure drop along the tube with the experimental data of Adelaja *et al.* (2017) at G = 400 kg/m^{2}s, and different inclination angles, saturation temperatures, and vapour qualities. As can be seen, the numerical results are highly

consistent with the experimental data, and show that the pressure drop increases with decreasing saturation temperature. This is because the kinematic viscosity of both the liquid, and vapour phases, increases with decreasing saturation temperature. Moreover, the effect of the inclination angle on the pressure drop along the tube is not significant at greater vapour qualities (x_m = 0.5 and x_m = 0.75), and can be attributed to the flow regime at high vapour quality. As discussed previously, the flow regime is approximately annular at higher vapour qualities; therefore, the shear stress force is more dominant than the gravitational force.

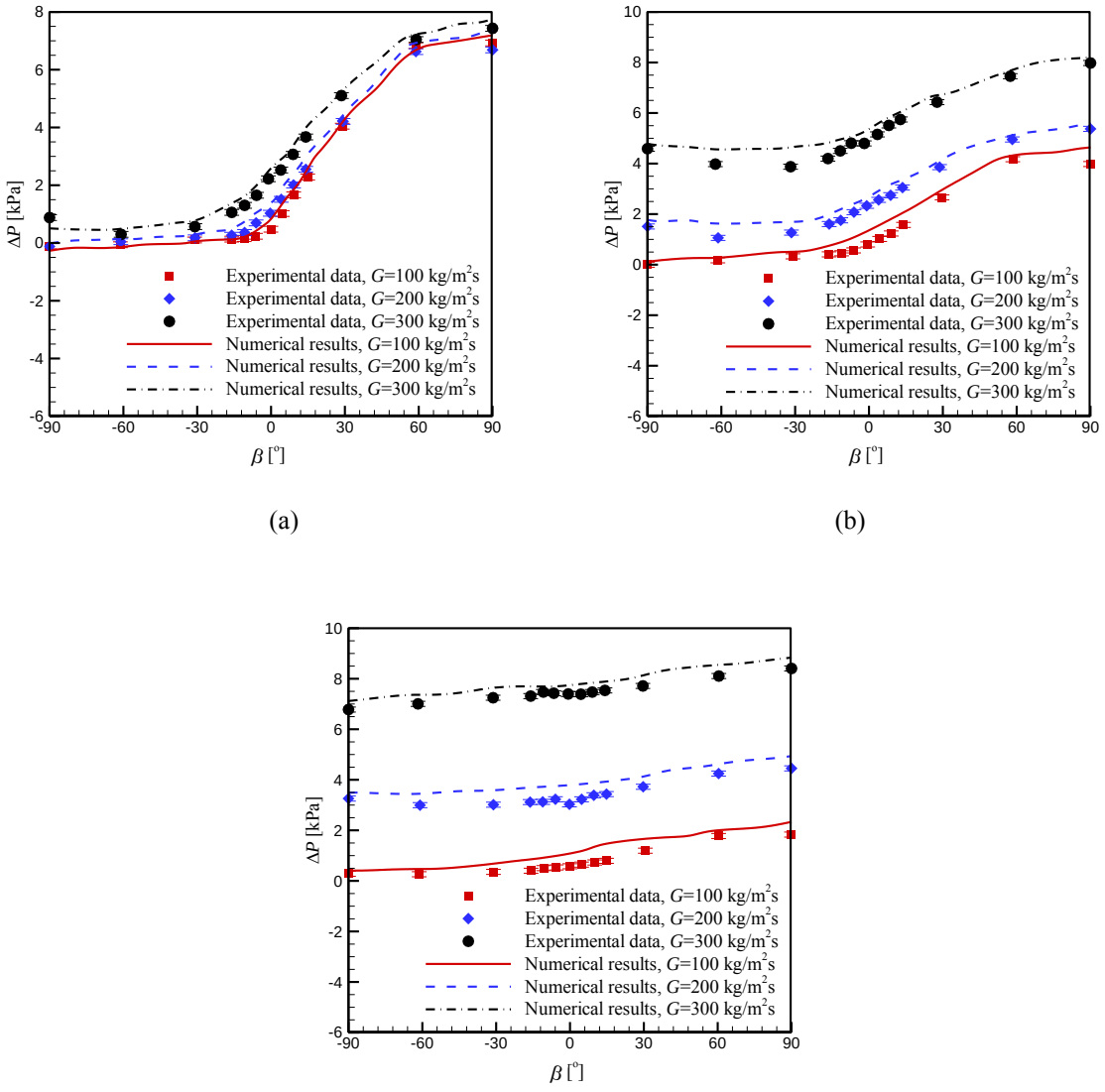

(a) (b)

(c)

Figure 16. Effect of mass flux on pressure drop along tube at T_{sat} = 30 °C, and different inclination angles: (a) x_m = 0.25, (b) x_m = 0.5, and (c) x_m = 0.75.

Similar results for the pressure drop along the tube at different mass fluxes and T_{sat} = 30 °C are presented in Figure 16. It is again observed that the numerical results are in good agreement with the experimental data of Adelaja *et al.* (2017) for different mass fluxes. The pressure drop along the tube increases with increasing mass flux, owing to increased velocity and the subsequent increase of the shear force inside the tube. Furthermore, with the increase in the vapour quality and mass flux, the flow regimes change to annular; therefore, the effect of the tube inclination angle on changes of the pressure drop decreases.

Figure 17 shows the effect of vapour quality on the pressure drop along the tube for T_{sat} = 30 °C, G = 300 kg/m^{2}s, and different inclination angles. The results show that the effect of the inclination angle on the pressure drop decreases with increasing vapour quality, as the flow regime is approximately annular at greater vapour qualities. In general, the pressure drops increase with increasing vapour quality, because of an increase in the shear stress. There are two specific cases, for x_m = 0.1 and x_m = 0.25 in the region of $\beta > 30°$, where the pressure drops increase with a decrease in vapour quality. This can be attributed to the fact that, in these two cases, the flow regime changes to churn-flow, that causes a significant increase in the pressure drop, indicating a significant interaction between the gas and the liquid phases (Owen, 1986). It is noteworthy that the flow regimes for all other cases with the corresponding operating conditions mentioned in Figure 17 are stratified, stratified-wavy, or annular.

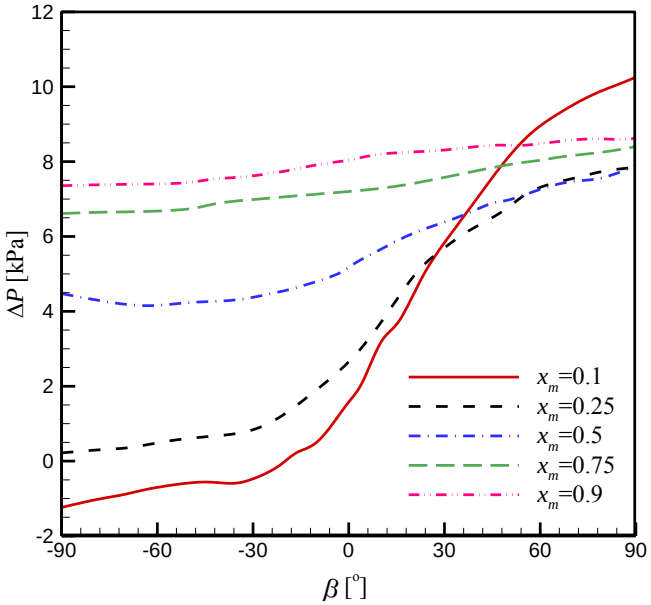

Figure 17. Effect of mean vapour quality on pressure drop along tube at T_{sat} = 30 °C, G = 300 kg/m^{2}s, and different inclination angles.

4.4.2. Frictional pressure drop

The effect of different parameters, such as refrigerant mass flux (Figure 18), mean vapour quality (Figure 19), and saturation temperature (Figure 20) on the frictional pressure drop along the tube is discussed in this section.

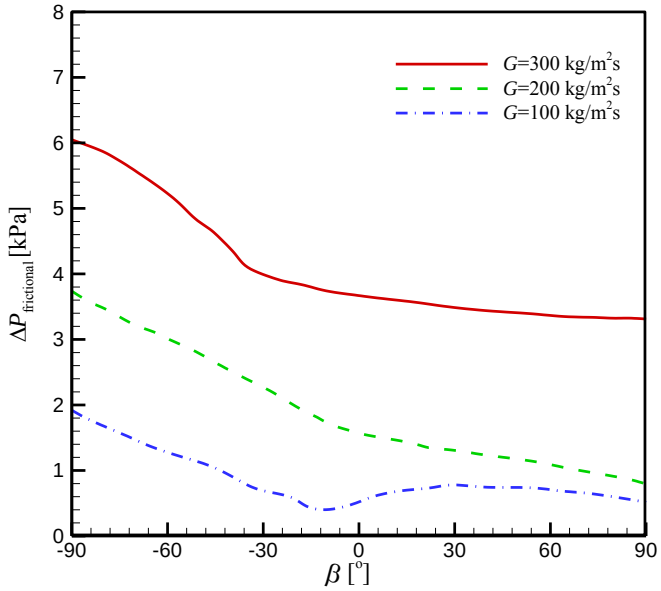

Figure 18. Effect of inclination angle on simulated frictional pressure drops for different mass fluxes at xm = 0.5 and T_{sat} = 40 °C.

The effect of mass flux on the frictional pressure drop as a function of inclination angle is shown in Figure 18 for the mean vapour quality of x_m = 0.5 and T_{sat} = 40 °C. As expected, it follows that the frictional pressure drops increase significantly as the mass flux increases from G = 100 to 300 kg/m^{2}s, as a result of an increase in the convection effect. As the frictional pressure drop is a direct function of the fluid velocity, increase of refrigerant mass flux increases the fluid velocity and consequently increases the frictional pressure drop. Contrary to the total pressure drop, the highest frictional pressure drops are obtained for vertically downwards flow. This can be attributed to the fact that, at this inclination angle, the effect of the assisting gravity force is the greatest, and results in an increase in the convection effect. With increasing tube inclination angle, the effect of the gravity force diminishes, and it opposes the flow at positive inclination angles. As a result, the frictional pressure drop decreases with increasing tube inclination angles.

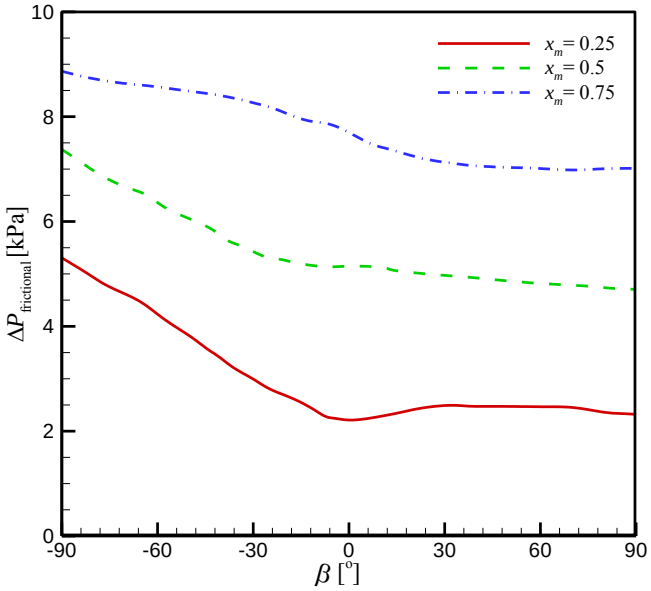

Figure 19. Effect of inclination angle on simulated frictional pressure drops for different mean vapour qualities at G = 300 kg/m^{2}s and T_{sat} = 30 °C.

In Figure 19, the effect of mean vapour quality on the frictional pressure drop is presented for G = 300 kg/m^{2}s and T_{sat} = 30 °C. The results show that, with the increasing mean vapour quality, the frictional pressure drop increases due to increasing shear stress. It can also be seen that, with an increase in the mean vapour quality, the effect of inclination on the frictional pressure drop becomes less dominant owing to the reduction in the liquid hold-up. Furthermore, the results show that the decrease in the frictional pressure drop is greater in downwards flow. This is because that, in upwards flow, the flow regime is approximately churn, in which the inclination has less effect on the condensation and pressure drop inside the tube.

Figure 20 illustrates the effect of saturation temperature on the frictional pressure drop for G = 400 kg/m^{2}s and x_m = 0.5. The general trend for the variations of the frictional pressure drop is similar to those of Figures 18 and 19, in which the frictional pressure drop shows a decreasing trend with increasing tube inclination angle. The results also show that increasing saturation

temperature causes a decrease in the frictional pressure drop along the tube. This can be attributed to the viscosities of both the liquid and vapour phases decreasing with increasing saturation temperature.

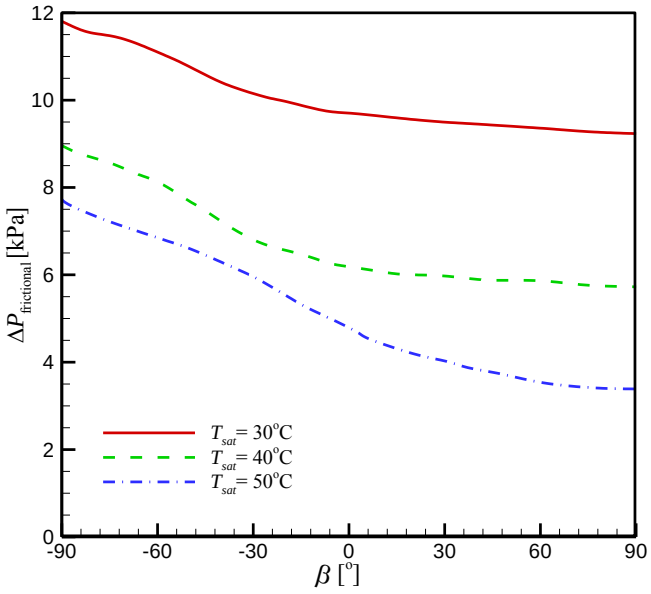

Figure 20. Effect of inclination angle on simulated frictional pressure drops for different saturation temperatures at G = 400 kg/m^{2}s and xm = 0.5.

5. Conclusion

This study presented a numerical simulation for the condensation of R134a inside an inclined smooth tube. The test case was a tube of length 1.488 m, and diameter 8.38 mm. The VOF model was utilised to express the governing equations. Previous experimental data were used for the validation of the numerical simulations. The results showed that the present numerical method could accurately capture the flow regimes in various operating conditions. The effect of the inclination angle on the heat transfer coefficient, and pressure drop, along the tube was observed to be lower at higher mass fluxes and vapour qualities. Under these conditions, the flow regimes are approximately annular, and the shear stress force is more dominant than the gravitational force. Furthermore, an optimum inclination angle region of -30° < β < -15° was

observed in the simulation, within which the condensation heat transfer coefficient was maximum. It was also found that the condensation heat transfer coefficient and pressure drop along the tube increased with increasing mass flux and vapour quality and with decreasing the saturation temperature. Furthermore, the results showed that the liquid film thickness, as well as the thermal resistance, increases along the tube and also with increase in the saturation temperature, which consequently cause a decrease in the condensation heat transfer coefficient.

Nomenclature

D	Tube diameter, m
e	Effective grid refinement ratio
E	Internal energy, J
F	Source term in momentum equation, Nm^{-3}
g	Gravitational acceleration, ms^{-2}
G	Mass flux, $kgm^{-2}s^{-1}$
GCI	Grid convergence index
h	Enthalpy, Jkg^{-1}
h_{ave}	Heat transfer coefficient, $Wm^{-2}K^{-1}$
j	Superficial velocity, ms^{-1}
j_v^*	Wallis superficial velocity
k	Thermal Conductivity, $Wm^{-1}K$
p	Pressure, Pa
q''	Heat flux, Wm^{-2}
r	Tuning coefficient, s^{-1}
R	Thermal resistance, KW^{-1}
s	Order of convergence

S_E	Energy source term, $Jm^{-3}s^{-1}$
S_l	Condensation mass source term, $kgm^{-3}s$
S_v	Evaporation mass source term, $kgm^{-3}s$
t	Time, s
T	Temperature, K
$\vec{u}$	Velocity, ms^{-1}
x	Vapour quality

Greek symbols

μ	Dynamic viscosity, Pa.s
v	Kinematic viscosity, m^2s^{-1}
ρ	Density, kgm^{-3}
k	Turbulent kinetic energy, $m^{-2}s^{-2}$
ε	Turbulent dissipation rate, $m^{-2}s^{-3}$
β	Inclination angle, degrees
ω	Contact angle at wall, degrees
θ	Circumferential angle, degrees
α	Volume fraction

Subscripts

ave	Average
b	Buoyancy
eff	Effective
l	Liquid
L	Laminar
m	Mixture
sat	Saturation

t	Turbulent
v	Vapour
wall	Tube wall

References

Abadi, S.M.A.N.R., Meyer, J.P., Dirker, J., 2018a. Effect of inclination angle on the condensation of R134a inside inclined smooth tube, Chemical Engineering Research and Design, 132, 346-357.

Abadi, S.M.A.N.R., Meyer, J.P., Dirker, J., 2018b. Numerical simulation of condensation inside an inclined smooth tube, Chemical Engineering Science, 182, 132-145.

Adelaja, A.O., Dirker, J., Meyer, J.P., 2016. Convective condensation heat transfer of R134a in tubes at different inclination angles, Int. J. Green Energy, 13, 812-821.

Adelaja, A.O., Dirker, J., Meyer, J.P., 2017. Experimental study of the pressure drop during condensation in an inclined smooth tube at different saturation temperatures, Int. J. Heat Mass Transf., 105, 237-251.

Beggs, D.H., Brill, J.P., 1973. A study of two-phase flow in inclined pipes, J. Pet. Technol., 25, 607-617.

Behafarid, F., Jansen, K.E., Podowski, M.Z., 2015. A study on large bubble motion and liquid film in vertical pipes and inclined narrow channels, Int. J. Multi. Flow, 75, 288-299.

Bortolin, S., Riva, E.D., Col, D.D., 2014. Condensation in a square minichannel: Application of the VOF method, Heat Transf. Eng., 35 193-203.

Brackbill, J.U., Kothe, D.B., Zemach, C., 1992. A continuum method for modeling surface tension, J. Comput. Phys., 100, 335-354.

Caruso, G., Giannetti, F., Naviglio, A., 2012. Experimental investigation on pure steam and steam-air mixture condensation inside tubes, Int. J. Heat Technol., 30, 77-84.

Caruso, G., Maio, D.V., Naviglio, A., 2013. Film condensation in inclined tubes with non-condensable gases: an experimental study on the local heat transfer coefficient, Int. Commun. Heat Mass Transf., 45, 1-10.

Chato, J.C., 1962. Laminar condensation inside horizontal and inclined tubes, ASHRAE J., 4, 52-60.

Col, D.D., Bortolato, M., Azzolin, M., Bortolin, S., 2014. Effect of inclination during condensation inside a square cross section minichannel, Int. J. Heat Mass Transf., 78, 760-777.

Darzi, M., Akhavan-Behabadi, M.A., Sadoughi, M.K., Razi, P., 2015. Experimental study of horizontal flattened tubes performance on condensation of R600a vapor, Int. Commun. Heat Mass Transf., 62, 18-25.

Diani, A., Cavallini, A., Rossetto, L., 2017. R1234yf condensation inside a 3.4 mm ID horizontal microfin tube, Int. J. Refrig., 75, 178-189.

Hirt, C.W., Nichols, B.D., 1981. Volume of fluid (VOF) method for the dynamics of free boundaries, J. Compt. Phys., 39, 201-225.

Höhne, T., Deendarlianto, Lucas, D., 2011. Numerical simulations of counter-current two-phase flow experiments in a PWR hot leg model using an interfacial area density model, Int J. Heat Fluid Flow, 32, 1047-1056.

Jr., G.G., Oliveira, J.L.G., Passos, J.C., 2015. Pressure drop during condensation of R-134a inside parallel microchannels, Int. J. Refrig., 56, 114-125.

Jung, D., Cho, Y., Park, K., 2004. Flow condensation heat transfer coefficients of R22, R134A, R407c, and R410a inside plain and microfin tubes, Int. J. Refrig., 27, 25-32.

Kaew-On, J., Naphattharanun, N., Binmud, R., Wongwises, S., 2016. Condensation heat transfer characteristics of R134a flowing inside mini circular and flattened tubes, Int. J. Heat Mass Transf., 102, 86-97.

Kang, Y., III, W.A.D., Hrnjak, P., Jacobi, A.M., 2017. Effect of inclination on pressure drop and flow regimes in large flattened-tube steam condensers, App. Therm. Eng., 123 498-513.

Kouhikamali, R., 2010. Numerical simulation and parametric study of forced convective condensation in cylindrical vertical channels in multiple effect desalination systems, Desalination, 254, 49-57.

Lee, W.H., 1980. A Pressure iteration scheme for two-phase flow modeling, multiphase transport: fundamentals, reactor safety, applications, Verizoglu, T. N., ed., Hemisphere Publishing, Washington, DC.

Lin, C., Wang, D., Bao, A., 2013. Numerical modeling and simulation of condensation heat transfer of a flue gas in a bundle of transport membrane tubes, Int. J. Heat Mass Transf., 60, 41-50.

Lips, S., Meyer, J.P., 2012a. Effect of gravity forces on heat transfer and pressure drop during condensation of R134a, Micro. Sci. Technol., 24, 157-164.

Lips, S., Meyer, J.P., 2012b. Experimental study of convective condensation in an inclined smooth tube. Part I: Inclination effect on flow pattern and heat transfer coefficient, Int. J. Heat Mass Transf., 55, 395-404.

Lips, S., Meyer, J.P., 2012c. Experimental study of convective condensation in an inclined smooth tube. Part II: Inclination effect on pressure drops and void fractions, Int. J. Heat Mass Transf., 55, 405-412.

Lips, S., Meyer, J.P., 2012d. Stratified flow model for convective condensation in an inclined tube, Int. J. Heat Fluid Flow, 36, 83-91.

Liu, Z., Sunden, B., Yuan, J., 2012. VOF Modeling and Analysis of Film wise Condensation Between Vertical Parallel Plates, Heat Transf. Research, 43, 47-68.

Meyer, J.P., Dirker, J., Adelaja, A.O., 2014. Condensation heat transfer in smooth inclined tubes for R134a at different saturation temperatures, Int. J. Heat Mass Transf., 70, 515-525.

Nebuloni, S., Thome, J.R., 2010. Numerical modeling of laminar annular film condensation for different channel shapes, Int. J. Heat Mass Transf., 53 2615-2627.

Nebuloni, S., Thome, J.R., 2012. Numerical modeling of the conjugate heat transfer problem for annular laminar film condensation in microchannels, J. Heat Transf., 134, 051021.

Nebuloni, S., Thome, J.R., 2013. Numerical modeling of the effects of oil on annular laminar film condensation in minichannels, Int. J. Refrig., 5, 1545-1556.

O'Neill, L.E., Park, I., Kharangate, C.R., Devahdhanush, V.S., V. Ganesan, I.M., 2017. Assessment of body force effects in flow condensation, part II: Criteria for negating influence of gravity, Int. J. Heat Mass Transf., 106, 313-328.

Olivier, S.P., Meyer, J.P., Paepe, M.D., Kerpel, K.D., 2016. The influence of inclination angle on void fraction and heat transfer during condensation inside a smooth tube

Int.l J. Multi. Flow, 80, 1-14.

Owen, D.G., 1986. An experimental and theoretical analysis of equilibrium annular flows, PhD Thesis, University of Birmingham, England.

Park, I., O'Neill, L.E., Kharangate, C.R., Mudawar, I., 2017. Assessment of body force effects in flow condensation, Part I: Experimental investigation of liquid film behavior for different orientations, Int. J. Heat Mass Transf., 106, 295-312.

Riva, E.D., Col, D.D., 2009. Numerical simulation of churn flow in a vertical pipe, Chem. Eng. Sci., 64, 3753-3765.

Roache, P.J., 1998. Verification and validation in computational science and engineering, Comput. Sci. Eng., 1, 8-9.

Shah, M.M., 1987. Improved general correlation for critical heat flux in uniformly heated vertical tubes, Int. J. Heat Fluid Flow, 8, 326-335.

Shah, M.M., 2016a. Comprehensive correlations for heat transfer during condensation in conventional and mini/micro channels in all orientations, Int. J. Refrig., 67, 22-41.

Shah, M.M., 2016b. A correlation for heat transfer during condensation in horizontal mini/micro channels, Int. J. Refrig., 64, 187-202.

Shah, M.M., 2016c. Prediction of heat transfer during condensation in inclined plain tubes, App. Therm. Eng., 94, 82-89.

Taha, T., Cui, Z.F., 2006. CFD modelling of slug flow in vertical tubes, Chem. Eng. Sci., 61, 676–687.

Tao, X., Nuijten, M.P., Ferreira, C.A.I., 2018. Two-phase vertical downward flow in plate heat exchangers: Flow patterns and condensation mechanisms, Int. J. Refrig., 85, 489-510.

Vadgama, B., Harris, D.K., 2007. Measurements of the contact angle between R134a and both aluminium and copper surfaces, Exp. Therm. Fluid Sci., 31, 979-984.

Vanderputten, M.A., Jacob, T.A., Sattar, M., Ali, N., Fronk, B.M., 2017. Two-phase flow regimes of condensing R-134a at low mass flux in rectangular microchannels, Int. J. Refrig., 84, 92-103.

Wallis, G.B., 1969. One-Dimensional Two-Phase Flow, McGraw-Hill, New York.

Wen, J., Gu, X., Wang, S., Li, Y., Tu, J., 2018. Numerical investigation on condensation heat transfer and pressure drop characteristics of R134a in horizontal flattened tubes, Int. J. Refrig., 85, 441–461.

Yan, Y.Y., Lin, T.F., 1999. Condensation heat transfer and pressure drop of refrigerant R-134a in a small pipe, Int. J. Heat ad Mass Transf., 42, 697-708.

Yang, Z., Shih, T.H., 1993. New time scale based k-ε model for near wall turbulence, AIAA J., 317, 1191-1197.

Yildiz, S., Duymaz, G., Ziegler, F., Auracher, H., 2017. Heat transfer during reflux condensation of R134a inside a micro-fin tube with different tube inclinations, Int. J. Refrig., 74, 425-434.

Zhuang, X.R., Chen, G.F., Zou, X., Song, Q.L., Gong, M.Q., 2017. Experimental investigation on flow condensation of methane in a horizontal smooth tube, Int. J. Refrig., 78, 193-214.